8-2004

Effect of Nanoscale Confinement on the Structure and Properties of Single Conjugated Polymer Molecules

Pradeep K. Koyadankizhakkedath
University of Tennessee - Knoxville

To the Graduate Council:

I am submitting herewith a dissertation written by Pradeep K. Koyadankizhakkedath entitled "Effect of Nanoscale Confinement on the Structure and Properties of Single Conjugated Polymer Molecules." I have examined the final electronic copy of this dissertation for form and content and recommend that it be accepted in partial fulfillment of the requirements for the degree of Doctor of Philosophy, with a major in Chemistry.

Mark D. Dadmun, Major Professor

We have read this dissertation and recommend its acceptance:

Michael D. Barnes, Robert J. Hinde, Jeffrey D. Kovac, Kevin M. Kit

Accepted for the Council:

Carolyn R. Hodges

Vice Provost and Dean of the Graduate School

(Original signatures are on file with official student records.)

To the Graduate Council:

I am submitting herewith a dissertation written by Pradeep K. Koyadankizhakkedath entitled "Effect of nanoscale confinement on the structure and properties of single conjugated polymer molecules." I have examined the final electronic copy of this dissertation for form and content and recommend that it be accepted in partial fulfillment of the requirements for the degree of Doctor of Philosophy, with a major in Chemistry.

Mark D. Dadmun,
Major Professor

We have read this dissertation
and recommend its acceptance:

Michael D. Barnes

Robert J. Hinde

Jeffrey D. Kovac

Kevin M. Kit

Accepted for the Council:

Anne Mayhew
Vice Chancellor and Dean of
Graduate Studies

(Original signatures are on file with official student records)

EFFECT OF NANOSCALE CONFINEMENT ON THE STRUCTURE AND PROPERTIES OF SINGLE CONJUGATED POLYMER MOLECULES

A Dissertation

Presented for the

Doctor of Philosophy

Degree

The University of Tennessee, Knoxville

Pradeep K. Koyadankizhakkedath

August 2004

To

My parents and my daughter

ACKNOWLEDGMENTS

I would like to thank Dr. Michael D. Barnes for his supervision and guidance throughout this research and am grateful for the opportunity to work in his lab space at the Oak Ridge National Laboratory where the ideas for this research was born and implemented. I would like to thank Professor Mark D. Dadmun for his guidance and intellectual stimuli during the course of this work. I would like to specially thank Dr. Adosh Mehta for his help with atomic force microscopy measurements and for his friendship and helpful discussions and Dr. Bobby Sumpter for molecular dynamics simulations. I also would like to thank Professor Robert Dickson and his group at Georgia Institute of Technology for their help with the simulations of emission pattern images. I would like to thank Professors Jeff D. Kovac, Robert J. Hinde and Kevin M. Kit for their help as members of my committee. I am also thankful to my family and friends for their support and encouragement during this work. Finally, I would like to thank the University of Tennessee, Department of Chemistry, Oak Ridge National Laboratory and Petroleum Research Fund for financial support and opportunity to carry out this research.

ABSTRACT

The research presented in this thesis was motivated by questions on the effect of nanoscale confinement on molecular conformation and related photophysical properties of conjugated polymers. Using microdroplet techniques as a method of isolating single molecules of various poly[phenylene vinylenes] we discovered that poly[2-methoxy-5-(2'-ethyl-hexyloxy)-1,4-phenylene vinylene] (MEH-PPV) and poly[2-Methoxy-5-(2'-ethylhexyloxy)-1,4-(cyanovinylene)phenylene] (CN-PPV) can be deposited on precleaned glass substrates with unique transition moment orientation. Structural investigation using a combination of fluorescence emission pattern imaging, atomic force microscopy and polarization anisotropy measurements revealed that individual polymer nanostructures had a high degree of intra-molecular with the long axis of the conjugated segment oriented perpendicular to the substrate. The high degree of internal structural order within individual polymer chains affected the spectral and photophysical properties compared to the bulk polymer. The photochemical stability of z-oriented nanostructures was orders of magnitude higher with ≈30x times more photon count rates than the in-plane oriented species in ambient conditions at similar excitation conditions. Z-oriented nanostructures showed narrow bandwidth spectral emission, which was typically redshifted with respect to the bulk polymer spectra. Investigation of the central frequency distribution of the fluorescence emission spectra of MEH-PPV revealed discrete emission from localized conjugated segments within the nanoparticle. Definitive evidence of single site emission from z-oriented polymer nanostructures was obtained from photon correlation measurements. Fluorescence lifetime and fluorescence quantum yield

measurements also point to a transition dipole surrounded by a nanoscale dielectric-in these case-conjugated segments in the polymer chain. With facile sample preparation, high photon count rates and high photochemical stability in the ambient conditions and highly pure single photon emission, z-oriented nanostructures can potentially be used as a source for single photon emission for quantum information processing.

TABLE OF CONTENTS

LIST OF TABLES

TABLE PAGE

LIST OF FIGURES

FIGURE PAGE

CHAPTER 1

Conjugated Polymers for Nanoscale Applications

1.1 Introduction

Molecular scale photonic and opto-electronic applications[1-4] of single molecules and nanostructures is one of the important areas in the rapidly developing field of nanotechnology. The use of conjugated polymers for nanophotonic and molecular scale optoelectronic applications can be conceived, considering the fact that these polymers are responsive to electrical and photonic excitations and has large number of light absorbing units per molecule[5], compared to their small molecule dyes, metal clusters or quantum dots.. Till now most of the research has been concentrated on thin films of conjugated polymers for electronic and photonic applications[6-8] However, there are serious technical challenges associated with the realization of these applications. One of the most important of them is the control of polymer chain morphologies[9-11], which in turn directly effects the photophysical properties and hence the ultimate application. In the single molecule regime, the molecular environment is much more critical than in the bulk in determining the photophysical properties.

However a series of experimental obstacle in utilization of conjugated polymers for nanoscale applications is the apparent pathological behavior of chain organization in solvent cast films. Because the chain organization of conjugated polymers is directly related to their spectral and photophysical properties, methods to optimize the performance of the end use product are currently the subject of intense research. To

understand the issues that affect the chain organization and the photophysical properties it is important to know the structural aspects of conjugated polymers. A discussion of the polymer systems used in this work will be useful to understand the above mentioned correlation between structure and photophysical properties.

Soluble derivatives of poly(paraphenylene) (PPV) are perhaps the most widely studied class of class of red emitting luminescent polymers.Used in a variety of applications[6,7]. Soluble derivatives poly[2-methoxy-5-(2'-ethyl-hexyloxy)-1,4-phenylene vinylene] (MEH-PPV) and Poly[2-Methoxy-5-(2'-ethylhexyloxy)-1,4-(cyanovinylene)phenylene] (CN-PPV) are particularly attractive because of their efficient luminescence and convenient solution processing (Figure 1). The presence of extended double bonds (π bonds) in the polymer backbone, give rise to both structural rigidity and optoelectronic properties. However, the polymer chain has a certain amount of flexibility due to the presence of flexible tetrahedral defects, twists and kinks in the polymer back bone[5] and is manifested in a persistence length that is much smaller than the contour length[5]. Any conjugated segment in the polymer backbone can act as a chromophoric site. The transition energy associated with chromophoric site is proportional to $1/L^2$, where L is the length of the chromophore. Thus, following from the persistence length of the polymer, as an approximation, the average conjugated segment (chromophoric box length., L) consists of 10-15 monomer units[12]. As a result depending on the number and nature of defects, a 100 kg/mol polymer can have 100 or more potential

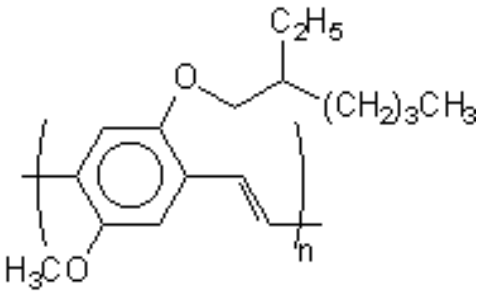

Poly[2-Methoxy-5-(2'-ethylhexyloxy)-1,4-phenylenevinylene] (**MEH-PPV**)

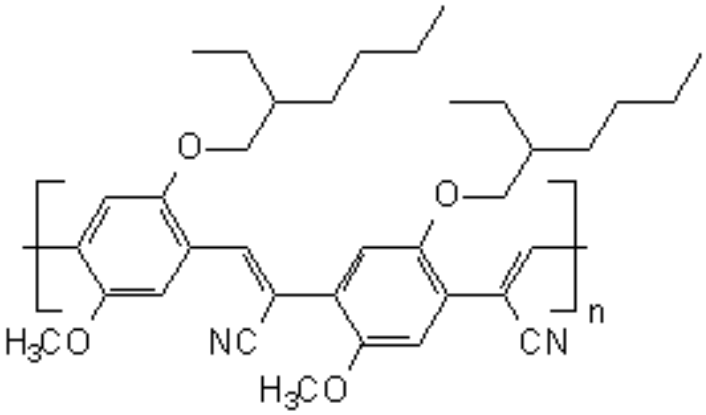

Poly[2-Methoxy-5-(2'-ethylhexyloxy)-1,4-(1-cyanovinylene)phenylene (**CN-PPV**)

Figure 1. Structure of MEH-PPV and CN-PPV.

chromophores per molecule. Since the defects are randomly distributed along the polymer chain, there is a distribution of conjugated segment lengths in the polymer chain. In films, the absorption maximum for both polymers are centered approximately at ~490 nm and the emission maxima are observed at ~575 nm and ~600 nm. The broad absorption and emission spectra are attributed to the presence of a large number of conjugated segments that can act as local chromophores within individual polymer chains. Since the polymer chain conformations affect the absorption and emission of the polymer, the absorption and emission maxima were found to shift in various solvents and in the bulk solid.

Depending on the nature and number of defects on the polymer backbone a polymer chain can adopt large number of distinct chain conformations[13]. First, the results of previous studies on the effect of chain morphologies on the spectral and photophysical properties in the bulk polymer[10,11,14,15] and then the results of previous single molecule studies[16-21] will be discussed. It has long been recognized that the photophysical properties of conjugated polymers depend strongly on their chain morphologies and their local environment[14,15,22,23].

Nguyen et al.[10,11,14,15,26] have published a series of papers investigating how the polymer chain morphologies affect the photophysical properties in the solid phase and in solution. Using different methodologies, they have shown the importance of polymer chain morphologies in determining the photophysical properties. They found that in the solid phase the emission wavelength is observed more towards the red wavelength as compared to that in solutions[10,11]. These shifts in the photoluminescence (PL) maximum are attributed to different polymer chain morphologies in different local environments.

The red shifted emission in thin films compared to the solutions is attributed to the more closely packed polymer chains in the solid, which in turn results in extensive π-π overlap between the conjugated segments of the polymer. The photoluminescence (PL) in different solutions also show spectra with PL maximua observed at different wavelengths depending on the chain conformations of the polymer. The PL maximum in a so-called "good" solvent (where the polymer chain conformation is extended due to favorable polymer-solvent interactions) is blue- shifted compared to that in a poor solvent[9,25]. In the "poor" solvents(where intra-chain interactions are more favorable than polymer-solvent interactions), individual polymer chains can adopt compact conformations, and considerable π-π overlap between conjugated segments of the same or different polymer chains manifest in spectral red-shifts as well as nonlinear optical effects[23].

In PL spectral measurements of MEH-PPV in dilute solutions of chlorobenzene (CB) and tetrahydrofuran (THF), Schwartz and coworkers[10] have observed a significant red-shift in CB relative to THF, a result consistent with light scattering data[10]. The dynamic light scattering data points to a more extended polymer chain conformation of MEH-PPV in CB relative to that in THF solution. That is, π-π overlap between the chromophores from different polymer chains in CB is considerable, as compared to that in THF and as a consequence the PL maximum is red shifted in CB compared to that in THF. Here, the lowering of the energy comes from π-π overlap between the chromophores from different polymer chains. This observation is in the opposite direction of what others have observed, where, a reduction in the solvent quality shifts the emission wavelength towards the red spectrum[25].

Collison et al.[25] have used nuclear magnetic resonance (NMR) and photoluminescence to study the effects of chain packing on the PL and PL quantum yield. They found that the reduction in solvent quality shifts the emission spectrum towards the red and also decreases the photoluminescence quantum yield. The reduction in quantum yield is attributed to the non-radiative decay in the excited state due to local order in the polymer chain. In good solvents, Collison et al. theorize that shorter effective chromophore lengths are observed as a result of torsional twists in the polymer backbone. They concluded that by changing the solvent-polymer interaction-vis molecular conformation-the solution phase photophysics can be controlled.

Even though extensive investigations have been carried out on the effect of polymer chain morphology, the effect of a single polymer chain conformation on the spectral and photophysical properties cannot be obtained from studies on the bulk polymer. Single molecule spectroscopy has been used as an effective tool to investigate the local environments in solids as well as to investigate the photophysical properties of the probe molecule[27-29]. In recent years, single molecule studies of MEH-PPV and similar polymers have improved the understanding of the relationship between their photophysics and chain morphology[17-20,30,31]. Single molecule studies have been used to investigate the nature of intra-chain aggregation in MEH-PPV and similar polymers.

Vanden Bout et al.[17] used single conjugated polymer molecules to study the energy migration between chromophores of a single conjugated polymer chain. They found out that the excitonic energy transfer takes place between different parts of a polymer chain (intra-molecular energy transfer). Excitonic energy migrates between

conjugated segments towards a fluorescence-quenching site created by reversible photochemistry of the polymer.

Tolbert and coworkers[16] investigated luminescence of MEH-PPV embedded in channels of mesoporous silica to demonstrate the intra-molecular energy transfer between chromophores in a conjugated polymer chain. They found that the energy migration occurred rapidly and efficiently from polymer chain segments lying outside the channels to the segments confined inside the channels. By modulating the input polarization they also found that the emission is linearly polarized along the silica channels indicating that the conjugated segments are oriented along the long axis of the channels. They also found that the energy migration along the polymer backbone inside the channels was less efficient than the energy migration from the conjugated segments outside the channels. Thus Tolbert and coworkers demonstrated that energy migration along the polymer chains can be controlled by the use of host-guest chemistry, where the polymer chains (the guest) were confined in nanoporous silica channels.

Barbara and coworkers[20] have used Monte Carlo (MC) simulations to model chain conformations of isolated, single molecules of MEH-PPV. The results of MC simulations suggest that the polymer molecules exhibit varying degrees of excitation polarization anisotropy that depend on the polymer chain conformation. The simulation results predicted that MEH-PPV polymer chains can adopt morphologically distinct families of configuration. They predicted different morphology classes named random coil, defect coil, toroid, defect rod etc. These different morphologies were detected using polarization anisotropy in the fluorescence. They also predicted different anisotropy distributions for different class of morphologies. Polarization anisotropy measurements

carried out on single molecules of MEH-PPV[20] dispersed in a polymer matrix using spin coating method yielded a broad distribution of chain conformations that were correlated with a mixture of random-coil-like geometries and weakly aligned structures. Although highly ordered cylindrical "rod" geometries were predicted, no experimental evidence of these interesting species has been reported in thin film formats. Thus polarization anisotropy measurement can be utilized as an effective tool to investigate the chain conformations of isolated single molecules of conjugated polymers. In addition a broad distribution of polarization anisotropy parameters in the thin films shows the lack of control over the chain conformations in the spin coating process.

In addition to polarization anisotropy measurements, other novel optical techniques have been used to interrogate molecular structure and the locality of radiative recombination within a single polymer chain. Recently Huser and coworkers[32] have observed non-classical photon statistics from single molecules of MEH-PPV prepared from specific solvents, indicative of luminescence originating from 2-3 (on average) chromophoric sites/molecule. This unique quantum optical signature was observed from samples prepared from toluene, while almost purely classical behavior was seen from single molecules prepared from chloroform. This indicates that polymer samples prepared from so-called "good solvents", where the chain configuration is expected to approximate a random coil, exhibit photophysical behavior representative of a multi-chromophoric system. This clearly indicates that the polymer chain conformations from solutions are preserved after the solvent is evaporated during the spin coating process.

Thus the chromophore organization in a polymer chain is the single most important factor in determining the excitonic energy transfer and quantum efficiency in

conjugated polymer molecules. However, methods to control the chromophore organization within individual polymer chains have been lacking to date and are important for utilizing conjugated polymers for nanoscale applications.

Previous work by Barnes et. al.[33,34] using microdroplet techniques combined with angle-resolved light scattering measurements has explored the process of phase separation of mixed polymer systems under three-dimensional confinement. Here, the role of droplet size and polymer mobility on the phase structure of mixed-polymer (dry) micro particles was found to be critical in determining the phase structure of the dry micro particle. Under conditions of rapid desolvation (< 1 ms), phase separation between two immiscible polymers was suppressed as a result of quenching the system in a homogeneous phase. Conversely, longer evaporation time scales resulted in phase-separation manifested by a distortion in the 2-dimensional light-scattering (diffraction) patterns. Barnes et. al.[35] have used microdroplets to isolate single molecules of Rhodamine 6G and investigate their photophysical properties.

In this thesis, I will discuss how single polymer chains (MEH-PPV and CN-PPV) can be isolated using droplet techniques and the chain conformations and chromophore organization in a single polymer chain can be controlled and investigated in the absence of a supporting polymer matrix. The organization of chromophores and the nature of the emissive site within individual polymer chains will be investigated using fluorescence emission pattern imaging, atomic force microscopy, polarization anisotropy measurement and photon correlation measurement. Ultimately the solution phase chain conformations will be correlated to the dry state conformation using a combination of fluorescence correlation spectroscopy (in the solution phase) and emission pattern imaging.

CHAPTER 2

Experimental

The goal of this research was to probe the morphology and spectral and photophysical properties of conjugated polymer molecules isolated from microdroplets of solutions in organic solvents. Using novel fluorescence imaging, spectroscopic, photon correlation and scanning probe techniques, we were able to learn the morphology and the photophysical properties of the single polymer molecules in the dry state, and how they differ from conventional film-based species. The experimental section is divided into two parts; the sample preparation and the investigation of the structural and photophysical properties using the above mentioned techniques. The sample preparation techniques were novel in their application to the materials under investigation. Fluorescence correlation spectroscopy (FCS) used to investigate the chain conformations of the polymer in the solution phase are discussed separately in chapter 5. In the present chapter we discuss sample preparation and spectroscopic methods.

2.1 Materials

The conjugated polymers used in this study, poly [2-methoxy-5-(2-ethyl hexyloxy)-p-phenylenevinylene] (MEH-PPV) and poly[2-methoxy-5-(2-ethylhexyloxy)-1,4-(1-cyanovinylene)phenylene] (CNPPV), were obtained from Sigma Aldrich chemical company and H. W. Sands corporation respectively. The MEH-PPV used in these experiments had a weight average molecular weight (M_w) of 135.5 kg/mol and a polydispersity index (PDI) of 1.06 and CN-PPV had an M_w of 100 kg/mol and a PDI of 5.2. The solvents, toluene, tehrahydrofuran (THF) and dichloromethane (DCM) were

bought from EM Sciences and were of OmniSolv^{TM} grade. The solvents and the polymers were used without further purification. Glass cover slips were obtained from Fisher Scientific (Fisherfinest^{TM} premium cover glass).

2.2 Sample Preparation

The sample preparation parameters were critical in determining the polymer chain morphology and the photophysical properties of the species under investigation. Hence a careful procedure was developed to isolate single polymer chains on the substrate. In order to prepare single molecules of conjugated polymer, a stock solution (10^{-7} M) of the polymer was made initially by dissolving the polymer in the solvent. The solution was further diluted in two steps to a concentration of 10^{-11}M. In each dilution step, the solution was sonicated thoroughly to make a homogeneous (at the molecular level) solution and to avoid any potential aggregation of the polymer chains. The solution was then set aside for two days before the samples were prepared. The optimum concentration was found to be between 10^{-11} and 10^{-12} M, which represents a balance between surface coverage and minimization of larger clumps containing multiple polymer chains.

The basic idea behind our sample preparation was to isolate single polymer chains in microdroplets of ultra-dilute solutions and deposit the individual polymer chains on glass substrates after solvent evaporation. To do this we used two sample preparation methodologies; one involves a piezoelectric droplet generator and the other involves nebulization of solution. In the first method a piezoelectric droplet generator similar in design to that used by Kung et al.[36] was used to isolate single polymer molecules in microdroplets. Figure 2 shows a schematic of the device. A Pyrex tube of 5 cm in length

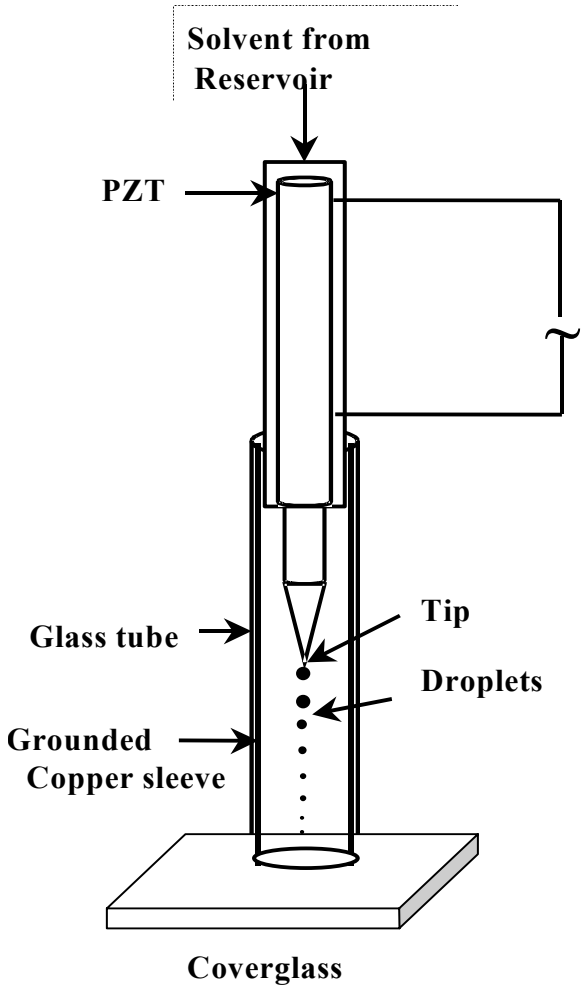

Figure 2. Schematic of piezoelectric droplet generator.

and 1 mm in diameter was fused at one end and was ground to yield a fine orifice of ~20 μm. The tip was then cleaned using THF and loaded with the dilute polymer solution. The quartz tip was then connected to the piezoelectric tube (PZT) and the solvent reservoir was filled with the solvent. The PZT was driven by an amplified analog pulse generator by approximately at a rate of ≈20Hz to produce micro droplets of roughly of the size of 5-10 μm. The droplet diameter was a function of the tip orifice diameter and the surface tension of the solvent. For the organic solvents used in our experiments, the tip orifice was ~20 μm. A higher orifice diameter was avoided to keep the solution droplet diameter below a critical value (~5μm) so that facile evaporation of the solvent was possible and to avoid clogging of the tip. The droplets dried en route to a glass substrate in a 15-30cm vented Pyrex tube. A grounded copper sleeve inside the glass tube was used to prevent electrostatic deflection of the charged droplets from stray charges on the inner surface of the glass tube. A flight distance of 15-30 cm assured that the droplets evaporated completely before encountering the substrate. Typically, samples were collected from the droplet generator for 3 hours, but the collection time varied (from 1 to 10 hours) depending on the desired coverage of polymer molecules on the substrate. The advantages of the piezoelectric generator were highly pure (in terms of molecular orientation) samples and control over the ejection of the droplets (on-demand). The disadvantages of the method were long sample collection times and frequent clogging of the orifice.

In the second method of sample preparation, nebulization of the sample solution was used to produce the microdroplets. In this method, a Pyrex tube (10 cm in length and

3 mm in diameter) was drawn on one end and was ground to yield an orifice of ≈ 20 μm, and was cleaned by sonication in THF. The non-tapered end of the Pyrex tube was immersed in the polymer solution. A high-pressure flow of high purity dry N_2 was used to nebulize the solution. A smaller orifice diameter and higher gas velocity results in smaller droplet diameter. A cover glass was held at a distance of 15-30cm away and perpendicular to the gas flow direction. Figure 3 is a schematic of the nebulization method. The nebulization was typically carried out for 30-45 seconds. Sample coverage was dependent on nebulization time and polymer solution concentration. Samples were prepared under similar conditions, including the same sample-substrate distance, gas velocity, deposition time, temperature and humidity. The choice of ideal solution concentration (10^{-11} to 10^{-12}M), a suitable substrate, ideal distance between the orifice and the substrate and small enough droplet diameter (<10 μm) was critical in producing samples of high quality. The advantage of this method over the piezoelectric method is quick sample preparation time, but this comes at the expense of sample 'impurities' (non-oriented molecules). Because of the ease of sample generation, the nebulization technique was used to prepare the majority of samples studied. Once the samples were prepared, they were investigated using optical probing techniques.

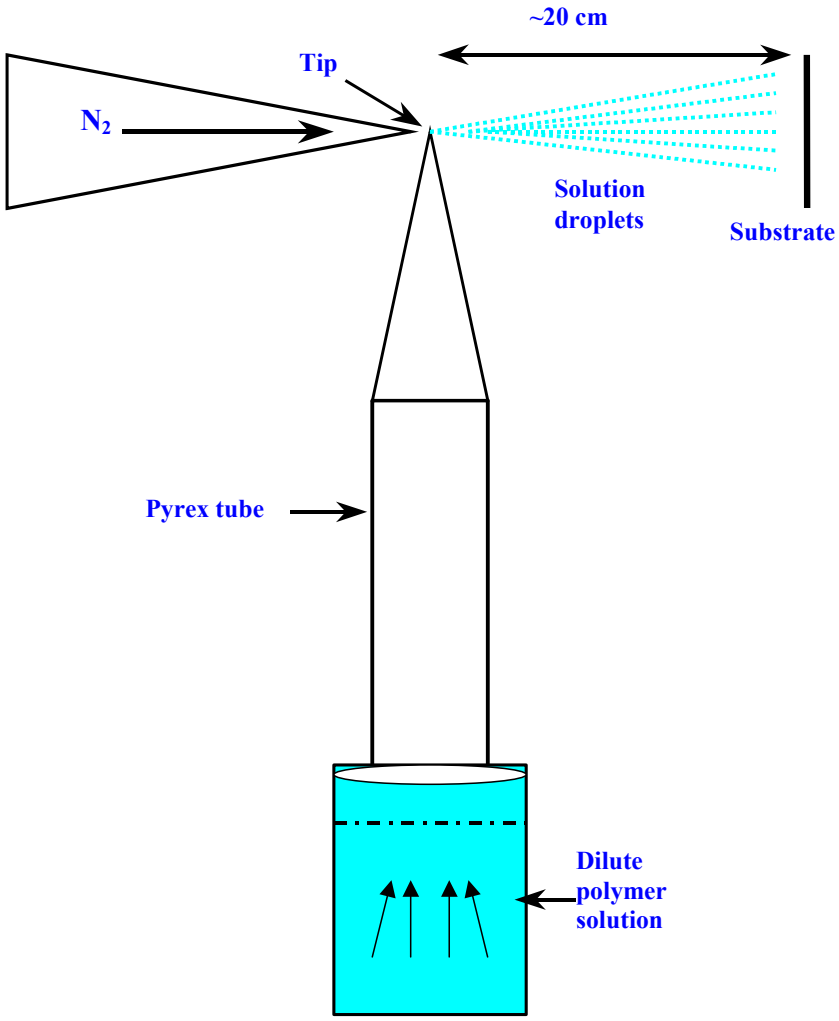

Figure 3. Schematic of spray nebulization.

2.3 Fluorescence Microscopy

Most of the optical measurements on dry polymer samples were made using a fluorescence microscope [Nikon Eclipse TE300]. Our microscope was configured to make several different measurements on the same platform with capabilities that include fluorescence emission pattern imaging of single molecules, fluorescence spectral measurements and topographical investigation of the sample using atomic force microscopy [Figures 4 and 5]. We used an intra-objective total internal reflection (TIR) configuration similar to that used by Dickson et al.[37] to investigate the 3 dimensional orientations of the transition dipoles, illustrated schematically in figure 4. In this configuration the laser beam (Argon ion laser, 514.5 nm) is brought-in slightly off axis. The laser beam undergoes total internal reflection at the coverglass-air interface. This generates an evanescent field at the coverglass surface as illustrated in the inset of figure 4 By controlling the polarization of the input laser beam it is possible to generate evanescent illumination field with non-zero intensity in the x, y and z cartaesian dimensions.

The fluorescence emission from the samples was collected for imaging, the light was diverted through the main viewing port of the microscope to a thermoelectrically cooled, high spatial resolution, high quantum efficiency (92% @600nm), back-illuminated frame transfer charge coupled device (CCD) camera (13μm, 512x512 pixels, Princeton Instruments EEV-57-10, read noise $4e^-$ rms) along with a 1.4 numerical aperture (NA) 100x objective and a 4x expander to give a real-space distance of 27 nm per pixel. The high (1.4) NA objective was necessary to collect the fluorescence emitted

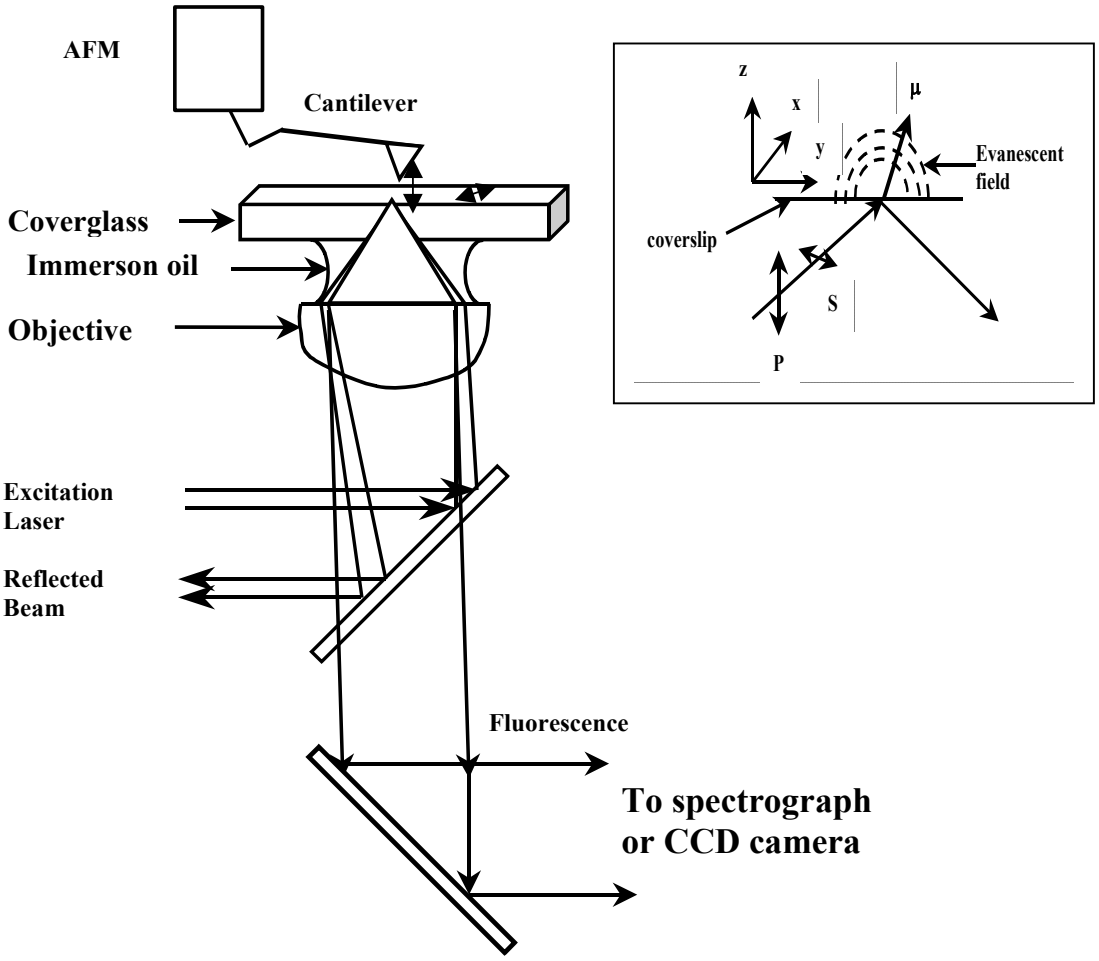

Figure 4. Microscope and TIR configuration (Inset). In the inset p and s polarization of the laser is depicted by double headed arrows.

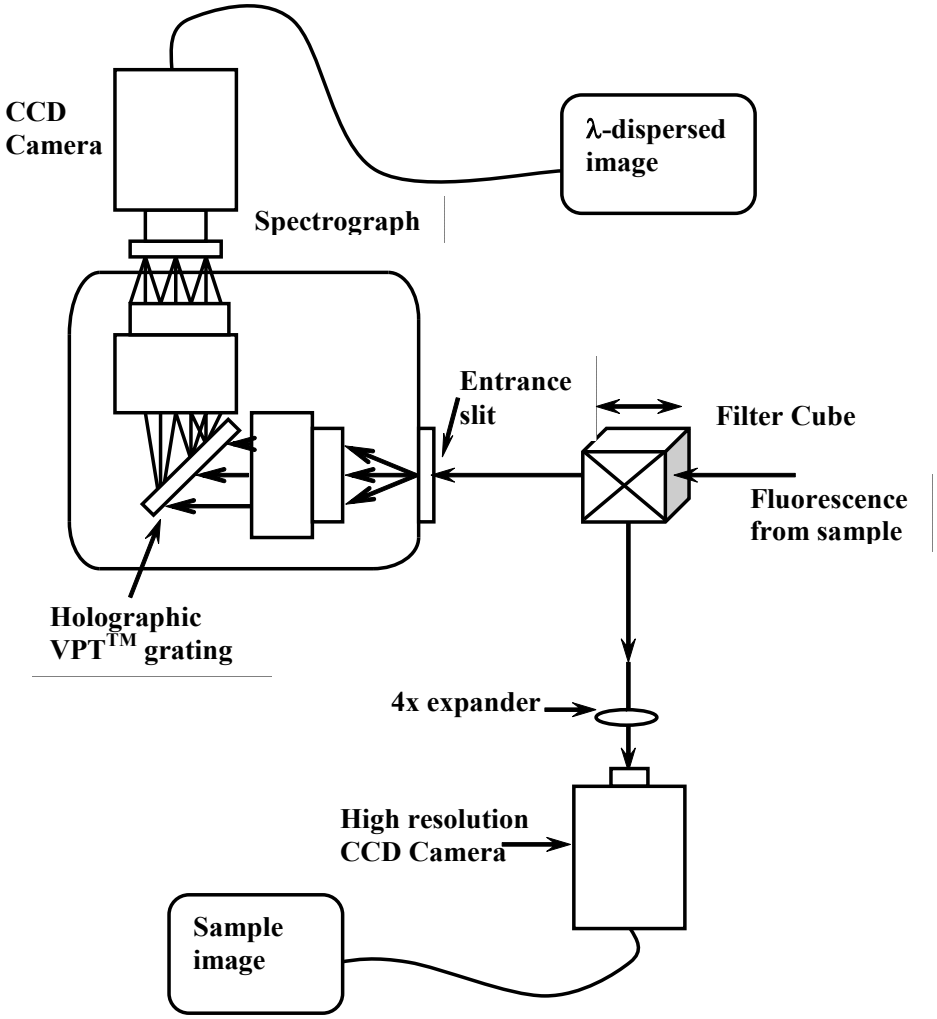

Figure 5. Schematic of spectrograph and high resolution CCD camera.

at high angles. Fluorescence was imaged through a dichroic filter and typically through a Corning long pass filter (590LP) although other filters were also used. An illumination intensity of 500 W/cm^2 was used for most experiments. High resolution, fluorescence pattern images of the molecules were recorded using the CCD camera. Precise dipole moment orientations were obtained by fitting the experimentally recorded emission patterns to a simulated image using computer codes generated at Georgia Institute of Technology by Kewei Xu. From the fitting, the polar angles θ and ϕ describing the orientation of the dipole can be obtained, with a precision of upto 1 mr depending on signal to noise ratio.

Fluorescence emission pattern imaging has been used as an efficient technique to probe three dimensional orientation of single dipoles[37,38]. The technique is based on the fact that molecules with single dipoles emit light with a sine-squared distribution relative to the dipole orientation. Figure 6 shows an example of emission pattern imaging using a single-chromophore molecule, DiI (1'-dioctadecyltetramethyl indotricarbocyanine Iodide, DiIC18) as a test molecule. DiI molecules embedded in poly (methyl methacrylate) (PMMA) matrix were used as control samples. A solution of DiI (10^{-8}M) and PMMA (10^{-4}M) in toluene was prepared and spin coated onto a coverglass. The sample was mounted on the objective with a drop of refractive index matching, immersion oil (Type DF, Cargill Inc) and focussed and defocussed images were obtained. Since the DiI molecules immobilized in the film have fixed dipole orientations, distinct emission patterns were observed corresponding to primarily in-plane (x-y) oriented emitters. Figure 6A shows the in-focus image of single DiI molecules dispersed in a PMMA thin film showing antenna emissions of in-plane oriented species. On slight

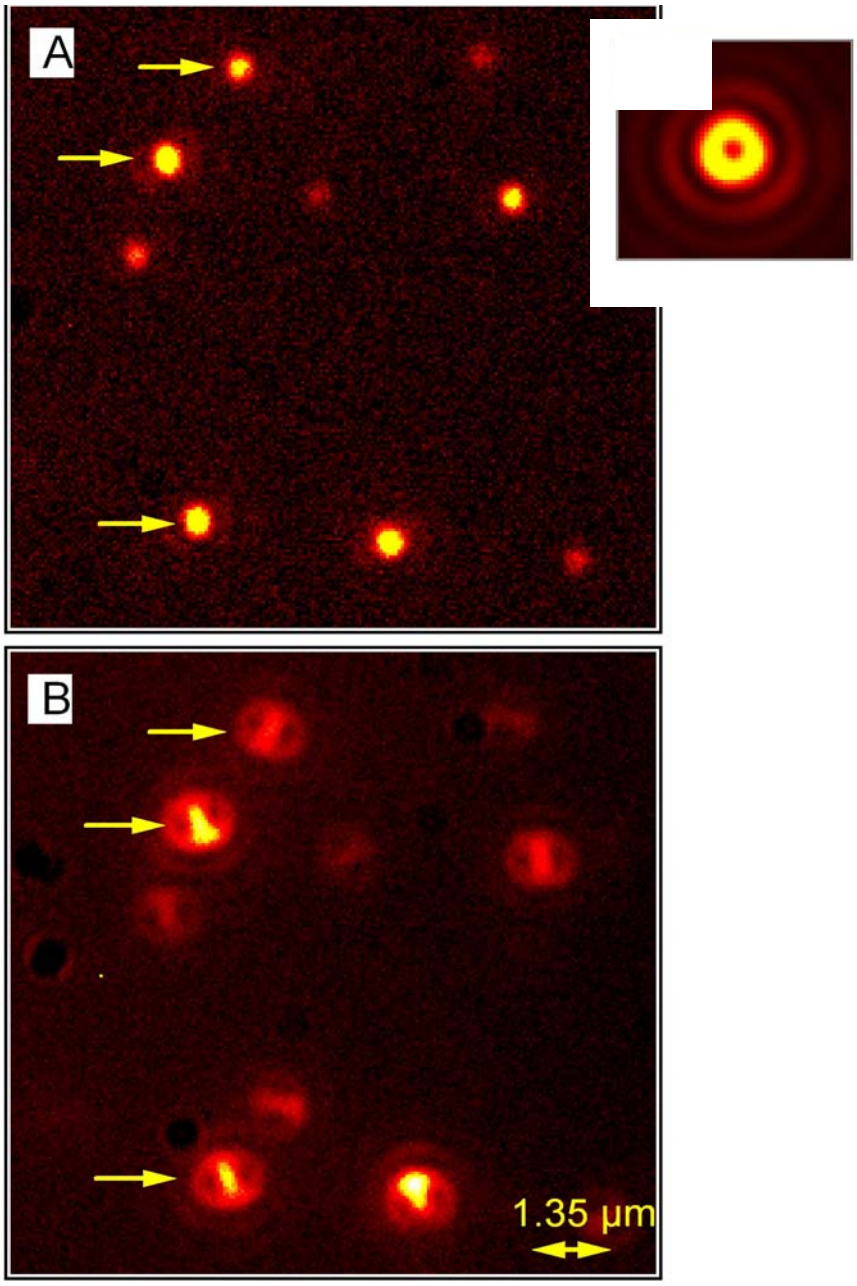

Figure 6. In-focus image of DiI single molecules (A), and the defocussed (~200µm) image (B). The arrows point to the same molecules. Image in top right panel (C) represents a single dipole oriented along the optic axis, showing 'donut'-like emission pattern are seen in DiI, but are minority species.

defocussing (~200μm) emission pattern images (Figure 6B) of the DiI molecules were obtained. The three arrows show the diffraction limited spots in figure 6A and the corresponding emission patterns on the defocussed image in figure 6B. The minor axis (of the ellipsoid) of the antenna patterns observed in figure 6B represents the approximate orientation of the dipole in the x-y plane. Molecules whose emission moments are not exactly parallel to the substrate show a distortion in the bright axis. The DiI molecules (and the dipoles) were randomly oriented in the plane (x-y) of the substrate. References 3 and 4 describe accurate theoretical modeling of the optical system which has enabled the precise fitting of dipole orientations in the z as well as in the x-y plane[37,38].

The emission patterns are uniquely defined by the orientation of the dipole in 3 dimensional (Cartesian) space. The formation of different emission patterns is graphically represented in figure 7. When in the focus of the microscope objective, the emission dipoles oriented in the substrate plane appear as diffraction limited spots (figure 7A). The family of rays emitted by the dipoles is focused by the objective resulting in a diffraction limited spot. On slight defocusing (~200nm) of the objective, a non-centro symmetric cat's eye-like pattern is observed (Figure 7B), which is characteristic of in-plane oriented dipoles. Light emitted at larger angles are collected by the high NA objective, resulting in an emission pattern with a bright axis and diffused wings around it. In the defocused image, the bright axis represents the dipole axis. Dipoles oriented along the optic axis emit light at high angles and were seen as toroid ('donut'-like) pattern with a dark node in the center (figure 7C). The 'donut'-like emission pattern can be observed on slight defocussing as well as in-focus.

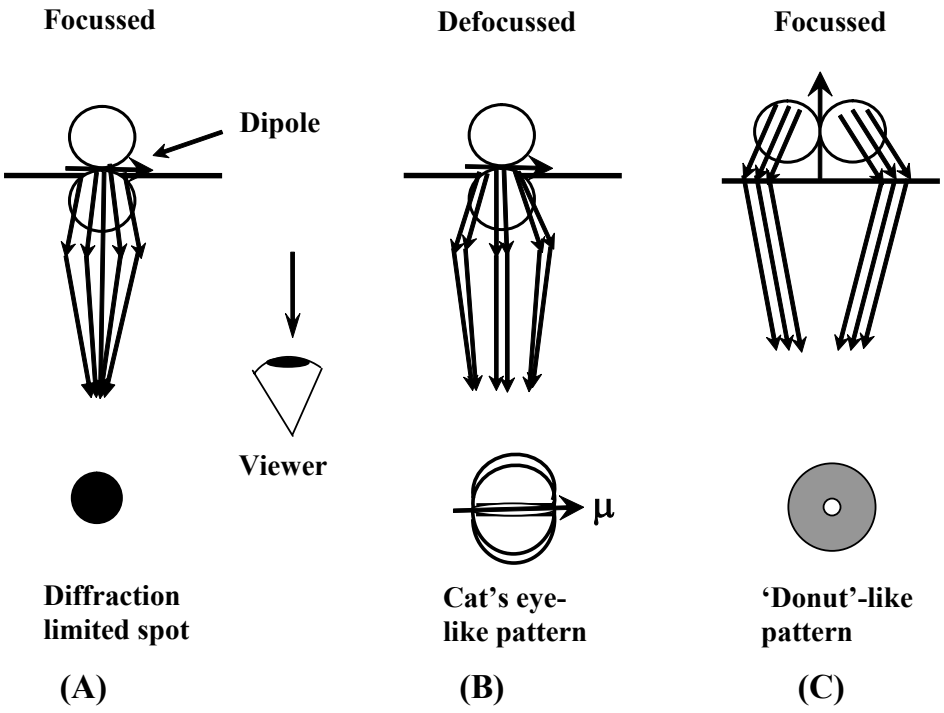

Figure 7. A graphic representation of the formation of characteristic emission patterns from single dipoles. When in focus (A) an in-plane oriented dipole appear as diffraction limited spot. Slight defocusing (B) of the objective result in a cat's eye-like pattern with central bar aligned along direction of the dipole. Dipole oriented along the optic axis (C) appears as a 'donut', with a dark node in the center. The 'donut'-like pattern is observed in-focus and well as on slight defocusing. When defocused slightly, additional diffraction rings are observed around the 'donut'-like pattern.

In our samples, we naturally observe z-oriented species as a consequence of the illumination geometryThis can be done by a variety of means: scanning near field, confocal or evanescent field excitation via total internal reflection. We used the TIR geometry to generate an evanescent electric field at the coverglass-air interface similar to that used by Dickson et al[37]. Under p-polarized excitation source the evanescent field carries significant polarization components in the z and y direction, with a reduced intensity in x.

2.4. Fluorescence Emission Spectra

For spectral measurements, the fluorescence was diverted through the side port of the microscope to a Holospec f/2.2 VPT^{TM} spectrograph (Kaiser Optics Inc., 50% transmission with holographic grating (HFG650), linear dispersion 12 nm/mm) and acquired using a back illuminated, high quantum efficiency (QE= 92% at 610 nm), thermoelectrically cooled CCD camera (Spec-10:400B, 20μm, 1340x400 pixels, read noise= 3.5 e^- rms). The spectrograph was calibrated using the emission spectra of a europium doped-yttrium oxide nanoparticle sample in which Stark components of the $^5D_0 \rightarrow {}^7F_2$ transition (λ=631, 611.56, 599 and 593 nm) provide unambiguous pixel-wavelength correspondence[39]. A spectral resolution of 0.2 nm/pixel was calculated using this method. This format allows us to correlate spectra with image and surface height information.

2.5 Atomic Force Microscopy (AFM)

A Digital Instruments Bioscope with Nanoscope III controller AFM scanner head mounted above the movable stage of the microscope was lowered to image the

topography or the size of the sample [Figure 4]. The AFM scanner was used in the tapping mode to obtain surface heights of the single molecules deposited on the glass substrate. In our configuration the silicon tip used in the AFM cantilever had a vertical resolution of ~1 nm and a lateral resolution of ~20 nm limited by tip radius. The microscope was located on a floating optical table to reduce mechanical noise in the AFM scan.

To correlate the size and the emission patterns, the AFM scan was performed on the same sample spot after the emission pattern images was obtained. The AFM scan area was calibrated using Nile red-doped 20 nm polystyrene beads[39]. Then the fluorescence image of the same sample region of the Nile red doped polystyrene was acquired. The AFM and fluorescence images were manually overlaid using graphing software (Igor-pro). From the overlaid image the extent of overlap between the scan area and the emission pattern was obtained and the offset, if any, was recorded. Once the offset was known the same procedure was followed for polymer samples to correlate the size with the emission patterns.

CHAPTER 3

Internal Structure and Orientation of Single Polymer Nanostructures

In this chapter we discuss the experimental probes of the intra-molecular structure of conjugated polymers isolated from microdroplets. As described in the previous chapter, our methodology involves isolation of single molecules of MEH-PPV or CN-PPV in microdroplets of dilute solutions and collecting the dry nanoparticles on glass coverslips. High resolution fluorescence emission pattern imaging was used to distinguish between multi or single dipole character and transition moment orientation. Comparing the fluorescence emission patterns of polymer molecules dispersed in thin films with the polymer nanoparticles prepared from microdroplet techniques led to the discovery that individual nanostructures uniform z-oriented transition moment can be oriented on glass coverslips when prepared from microrodroplets of dilute polymer solutions[40,41].

The mechanism of this intriguing orientation as well as spectral and photochemical differences are important questions addressed in this chapter. The structural information of the z-oriented polymer molecules was obtained by atomic force microscopy (AFM) and polarization anisotropy measurements. AFM measurements carried out on z-oriented nanoparticles revealed particle heights that range between 8-11 nm with the most probable height ≈10 nm. This distribution is in agreement with the persistence length (normal chromophore dimension) and leads to a picture of collapsed

polymer chains with the chromophore axis perpendicular to the substrate. This o collapsed (folded) and oriented nanostructure was further supported by hybrid molecular mechanics simulations of individual polymer chains with flexible tetrahedral defects. The polymer chains were found to fold at the tetrahedral defects and form a cylindrical structure under sample preparation conditions.

The orientation mechanism was believed to be electrostatic in nature, where the negative charges formed on the polymer chain during microdroplet production[42] interacting with random with random negative charges present on the glass coverslip. Electric force microscopy (EFM) measurements carried out on nebulized nanoparticles revealed a net negative charge on individual nanostructures. Surface modification (metal deposition, acid treatment and silylation) of the glass substrate by different was found to be unfavorable for the z-orientation of nanoparticles, consistent with a picture requiring anionic surface moieties for z-orientation. Contact angle measurements on modified coverslips indicated that the orientation of the nanoparticle was highly sensitive to the surface energy of the substrate.

3.1 Emission Pattern Imaging

Fluorescence emission pattern imaging was used to probe the local nature of emissive sites in single molecules of MEH-PPV and CN-PPV prepared using microdroplet techniques. As shown by the examples in chapter 2, fluorescence from single-dipoles results in a spatial intensity pattern uniquely defined by its orientation. However the test molecule (DiI) that has only a single chromophore per molecule, the polymer molecules under investigation were composed of as many as 100 local

chromophores[5]. However, depending on the polymer chain conformations, the number of actual emissive sites/molecule can vary, indeed some circumstances[17,19,30,32] appear single chromophoric in many regards. If the molecules under investigation were single-dipole emitters, depending on the dipole orientations, distinct spatial fluorescence intensity patterns, with unique transition dipole orientation should be observed from individual molecules.

As a control experiment, emission patterns from a spin coated sample of MEH-PPV single molecules on a coverglass were acquired. The single molecules were embedded in a PMMA thin film to enhance the photostability of molecules. Figure 8 shows a defocused image of MEH-PPV single molecules embedded in PMMA matrix. It can be noted that the molecules in Figure 8 show wide range of emission patterns, ranging from isotropic spots to well defined antenna emissions. Figure 8 clearly shows that spin coating results in predominantly in-plane (B) dipole orientation of the polymer molecules, with a significant fraction of multichromophoric species (C). In defocused image multichromophoric molecules appear symmetric and single chromophoric molecules appear as antenna patterns. The predominant species observed were intensity patterns representative of dipoles oriented in the x-y plane. The observation of antenna patterns from MEH-PPV single molecules indicates that the emission is localized within the polymer molecule. Some of the molecules appear as diffraction limited spots indicating random orientation of multiple chromophores within single polymer chains.

Since emission pattern imaging was used to determine the nature of emissive site in single polymer chains, precautions were taken to avoid the formation of multiple chains or clumps in the sample. An ultra-dilute solution concentration ($\leq 10^{-11}$M) was

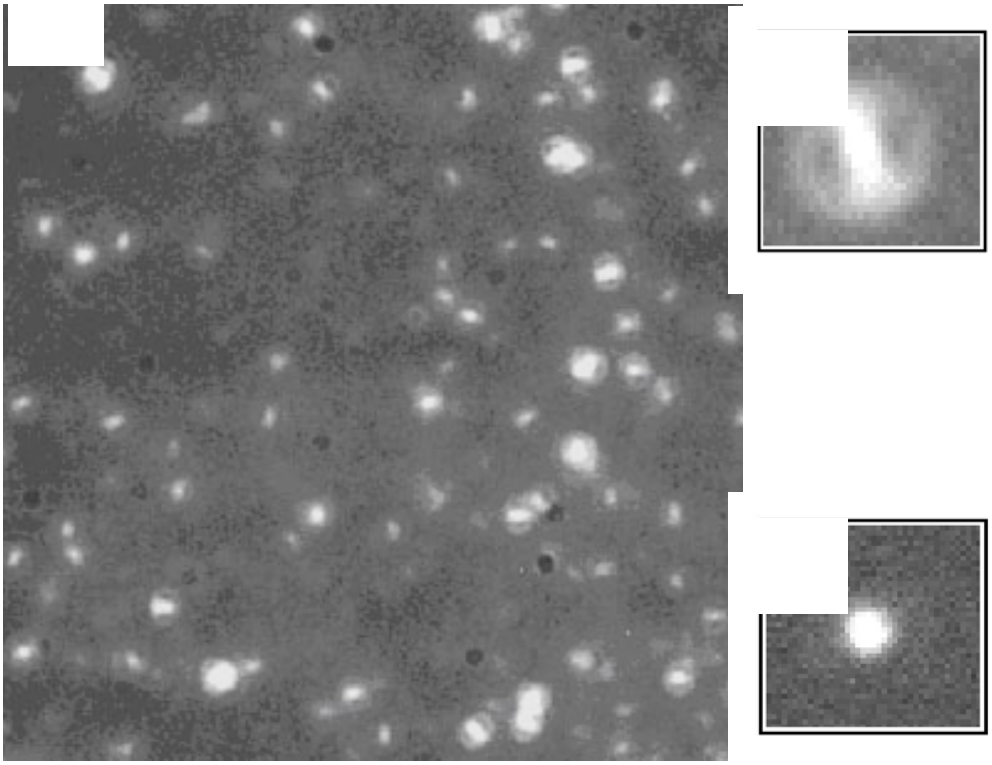

Figure 8. Fluorescence emission patterns of MEH-PPV single molecules dispersed in a PMMA matrix by spin coating from a THF solution. The close-up image of (B) a molecule with the dipole in oriented in the x-y (substrate) plane and (C) a multichromophoric molecule that appears like diffraction limited spot.

used to assure the deposition of single molecules. Assuming an initial droplet diameter of 10μm, a solution concentration of 1 pM corresponds to an average number of approximately 10^{-2} molecules per droplet. That is approximately 100 droplets contain a molecule. Further, the observation of on-off blinking[17,19] and discrete photobleaching combined with single-dipole emission patterns strongly suggests that the nanoparticles were single polymer chains. Further evidence for the single molecule behavior comes from photon antibunching measurements, described in the next chapter.

Figure 9 shows the high resolution spatial fluorescence intensity patterns of MEH-PPV [9A] and CN-PPV [9B] single molecules, prepared from microdroplets of toluene solutions. It can be seen that all of the molecules in figure 9 show 'donut'-like emission patterns, characteristic of single-dipoles aligned parallel to the optic axis (perpendicular to the glass substrate). The toroidal spatial intensity patterns seen both in focus as well as in slight defocusing can be understood from the fact that emission is forbidden at angles along the optic axis for *z*-oriented dipoles, resulting in the central intensity node for a given nanoparticle fluorescence image. As an approximation, the body fixed axis of the dipole (and the molecule in case of a single chromophore) is taken to be in the central dark node of the 'donut'-like pattern. The observation of z-orientation was the exact opposite of the dipole orientation of MEH-PPV in spun-cast thin films that lie randomly oriented (in ϕ) nearly parallel to the substrate.

The emission patterns observed in figure 9 were observed from single molecules of MEH-PPV [9A] and CN-PPV [9B]. Some of the images in figure 9 have slight asymmetry in the emission pattern that derives from a small tilt in the dipole orientation relative to the normal. Figure 10 shows emission pattern images of z-oriented MEH-PPV

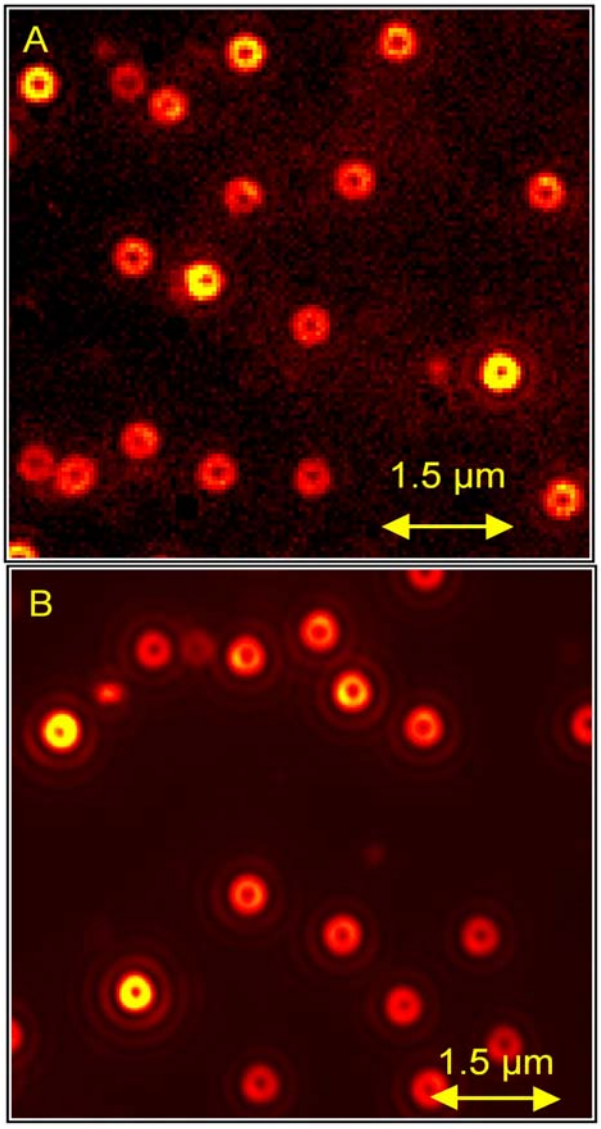

Figure 9. Fluorescence emission pattern images of (A) MEH-PPV and (B) CN-PPV single molecules deposited on glass substrate using nebulization from dilute polymer solution.

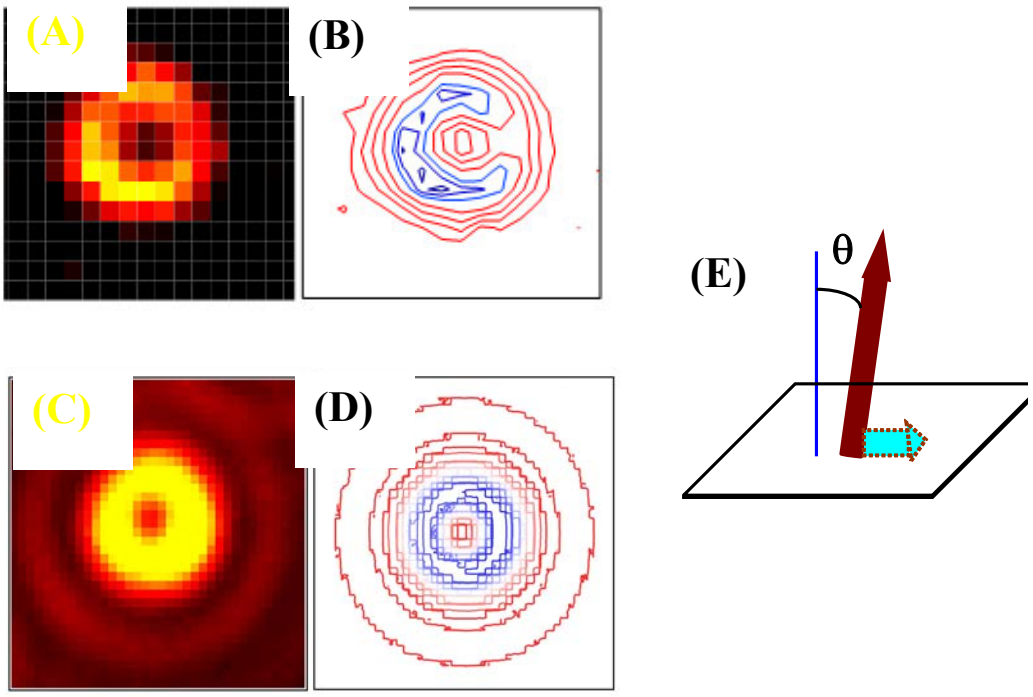

Figure 10. Observed (A and C) and simulated (B and D) intensity patterns of z-oriented MEH-PPV and CN-PPV nanoparticles respectively. From the intensity distribution the tilt angle of the emission dipole with respect to the surface normal was calculated. In the present example, tilt angles (θ) of 3.5° and 1° was observed for MEH-PPV and CN-PPV respectively. The bottom panel (E) is a representation of a tilted (θ) dipole with respect to the surface normal and its projection on the x-y plane. Images (A) and (C) were acquired under different conditions resulting different image contrasts.

and CN-PPV molecules (A and C) and patterns generated using classical electrodynamics, shown in contour image plot (B and D). The precise fitting of the 2-D spatial intensity patterns[37] of MEH-PPV and CN-PPV indicate dipole tilt angles of 3.5° and 1° with respect to the surface normal [The fitting of the 2-D spatial intensity patterns were carried out in Prof. Rob Dickson's group at Georgia Institute of Technology by Kewei Xu]. Even though emission pattern imaging does not yield any direct information about the structure of the macromolecule, the fact that all the dipoles in figure 9 were oriented perpendicular to the substrate leads naturally to a picture where molecules are collapsed and have a folded, cylindrical structure. Without a high degree of structural order, transition moment orientations would be expected to be more or less random. The concept of a folded, intramolecular geometry was supported by molecular dynamics simulations performed by Bobby Sumpter at the Oak Ridge National Laboratory. Figure 11 shows an example of folding trajectory of a CN-PPV nanostructure obtained by one of such simulations.

3.2 Atomic Force Microscopy Measurements

To test the idea of folded geometry we explored the structure using AFM. Particle heights of the nanostructures were measured using tapping mode AFM and a histogram of particle height distribution was constructed with 1 nm precision in z, while lateral features (in x,y) were obscured by the tip radius (≈25 nm). Thus the aspect ratio of the nanoparticles could not be obtained directly, but could be inferred from a combination of z and in-plane oriented measurements. Figure 12 shows AFM surface height images for z-oriented (12A) and in-plane (12C) CN-PPV samples along with the histogram of

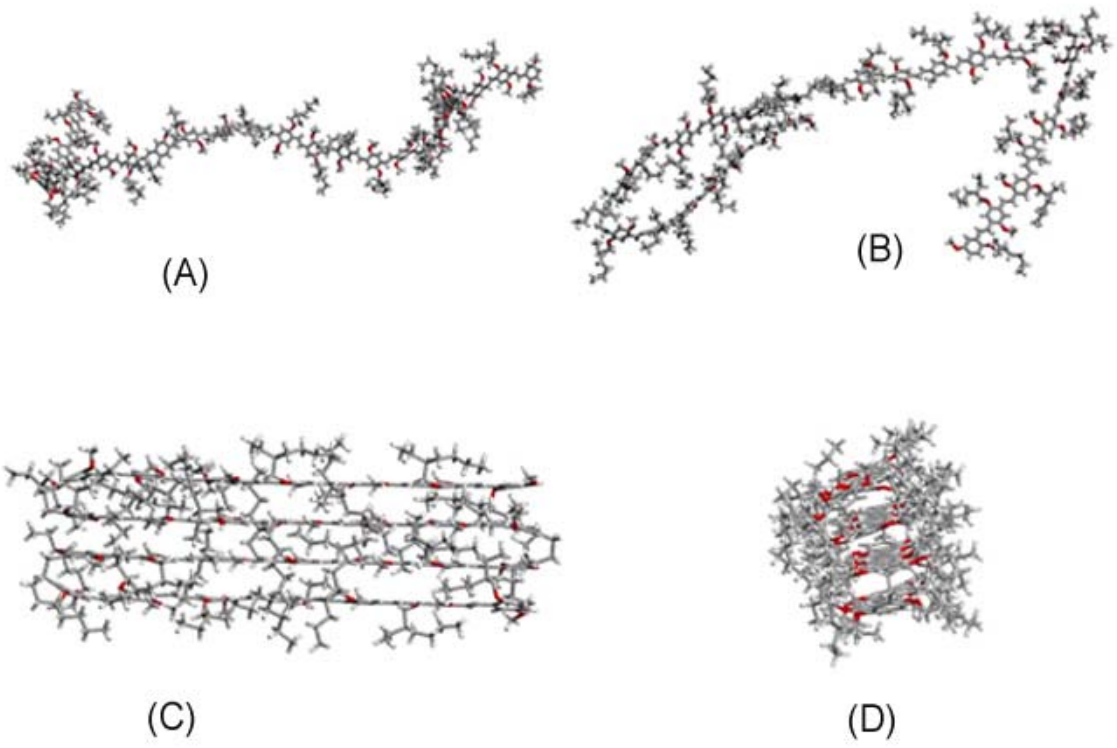

Figure 11. Folding trajectory of a CN-PPV oligomer. The minimum energy structures are folded at the tetrahedral defect.

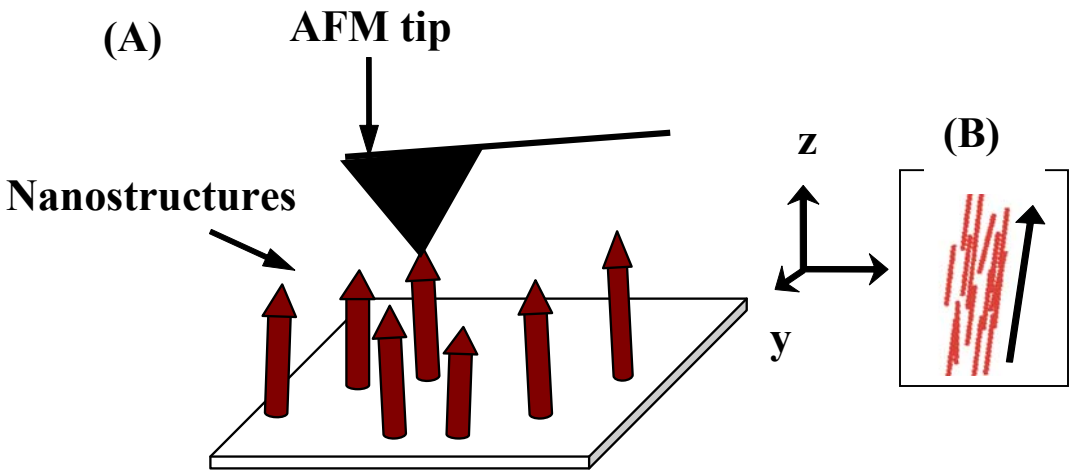

Figure 12. A schematic representation of z-oriented polymer nanostructures and height measurement using AFM (A). The schematic in (B) represent crude approximation of chromophore organization within a nanoparticle.

measured particle heights. Both samples were prepared under similar conditions using nebulization technique from the same solution. For the z-oriented sample, the particle height distribution peak was found around 10 nm. These values were in good agreement with the persistence length of PPVs measured by dynamic light scattering techniques[5]. The persistence length of MEH-PPV was measured by Gettinger et al.[5] by light scattering techniques and is a measure of the flexibility of the polymer chain. In our system the persistence length can be approximated to the length of a chromophore, which is typically composed of 10-15 monomer units. For CN-PPV nanoparticles that were oriented in the plane of the substrate (in this case, mica) the surface height distribution ranges from 1 to 3 nm with a mode of 1.67 nm. This means that the molecules were almost exclusively lying on the substrate plane with the chromophores predominantly in the substrate plane. An aspect ratio ($\langle h_z \rangle / \langle h_{in\text{-}plane} \rangle$) ≈ 5 can be inferred from the two measured height distributions. All the AFM and EFM measurements were carried out by Adosh Mehta at the Chemical Sciences Division, Oak Ridge national Laboratory.

Measured particle heights for z-oriented MEH-PPV molecules were in the range of 5-15 nm with a distribution maximum of about 8 nm. Note that this is comparable to persistence length, much smaller than the contour length, suggesting folded, cylindrical nanostructure. Because the transition moment for poly(phenylene vinylenes) is nearly collinear with the conjugation axis[16,43], the uniformity in the transition moment orientation combined with structural information from AFM suggests a folded cylindrical nanostructure for both CN-PPV and MEH-PPV, with the long axis oriented perpendicular to the substrate similar to the structure predicted by molecular dynamics simulations carried out by Bobby Sumpter. Figure 13 helps illustrate this scenario. The solid arrow in

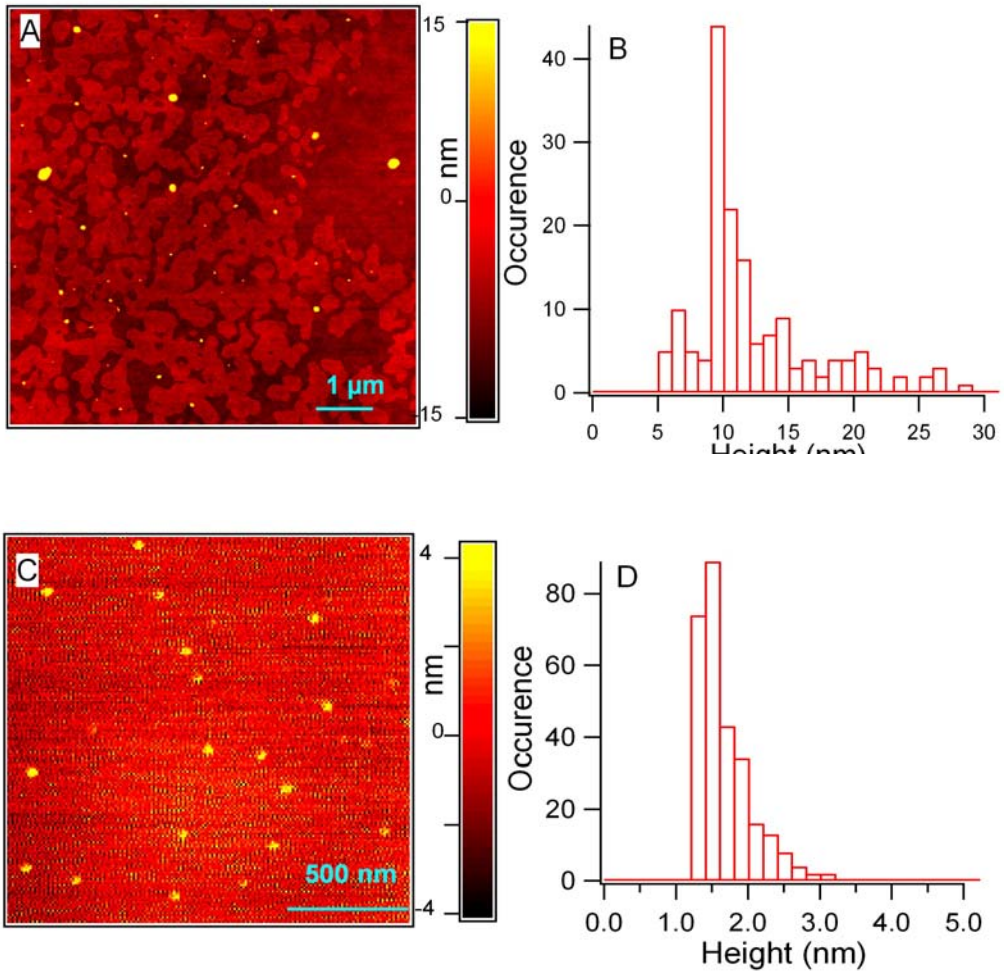

Figure 13. (Top) AFM image of (A) z-oriented CN-PPV single molecules and (B) surface height distribution with maximum at 10.6 nm. (Bottom) AFM image of (C) in-plane CN-PPV single molecules deposited on mica substrate and (D) surface height distribution with a maximum of 1.67 nm. Both samples were nebilized from same solution. Ratio of $\langle h_z \rangle / \langle h_{in\text{-}plane} \rangle$ provides estimate of aspect ratio of ≈5.

figure 13 B represents the dipole orientation and the red rods represent individual chromophores. The conjugated segments are connected together by covalent bonds (not shown).

Figure 14 shows the correlation between the z-oriented MEH-PPV single molecule fluorescence emission pattern and the corresponding AFM image. The four particles range in size from 7-12 nm. The correlated height information with the fluorescence image and the particle height distribution from figure 14 clearly shows that the 'donut'-like emission patterns observed in the case of single polymer molecules originate from collapsed and oriented molecules with the chromophore axes oriented perpendicular to the substrate.

3.3 Electric Force Microscopy

The uniform z-orientation observed in microdroplet generated samples can be explained in terms of an electrostatic interaction between the nanoparticle (as a charged, cylindrical nanostructure) and stray charges on the glass surface. The small excess charge on the particle was produced during droplet ejection from the quartz orifice and the charge carriers remain on the particle after solvent evaporation[42]. If the nanostructures were cylindrical (with carriers localized on the external surface), the electrostatic energy of the system would be minimized by orienting the molecule with the long axis perpendicular to the substrate. Electric force microscopy (EFM) was used to interrogate the charge state of nebulized nanostructures to test this idea. Figure 15 shows an EFM image for Z-oriented CN-PPV molecules prepared from toluene using nebulization technique. The charge image was generated by measuring the shift in cantilever frequency as a result of the long range electrostatic forces. Contrast in the image stems

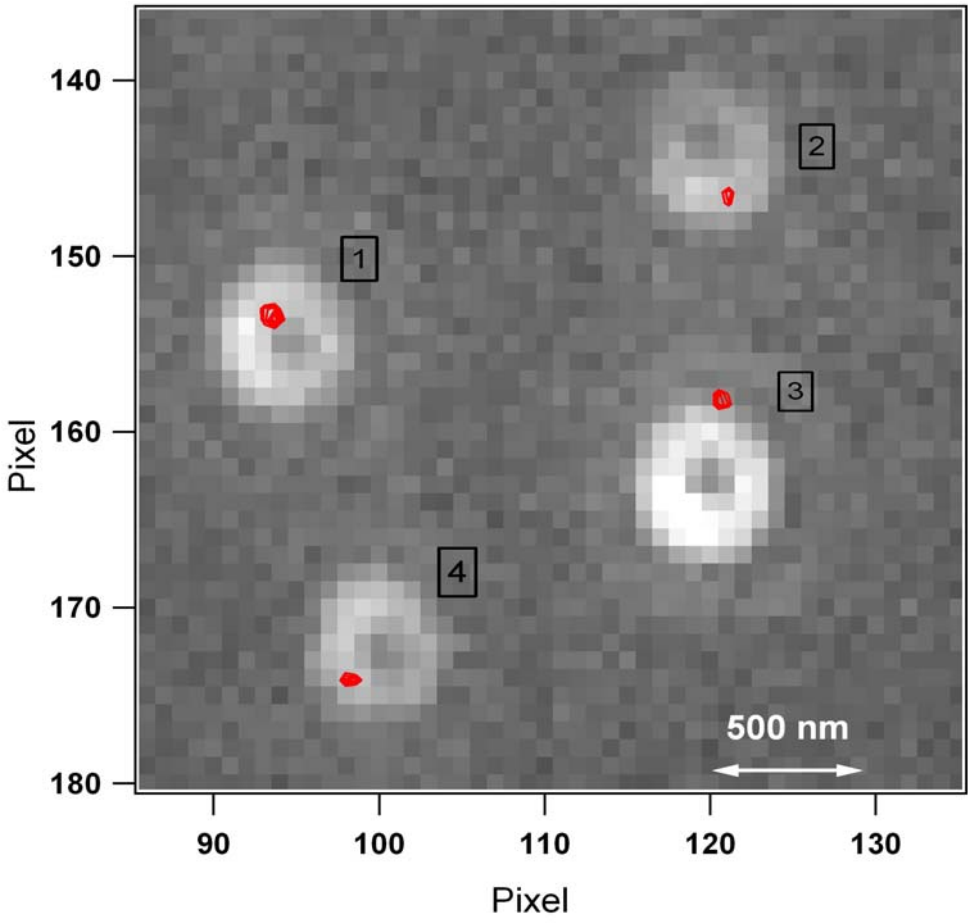

Figure 14. Size correlation between the fluorescence emission pattern and AFM image of z-oriented MEH-PPV single molecules. The red contours are tapping mode AFM image of the same area as the fluorescence image.

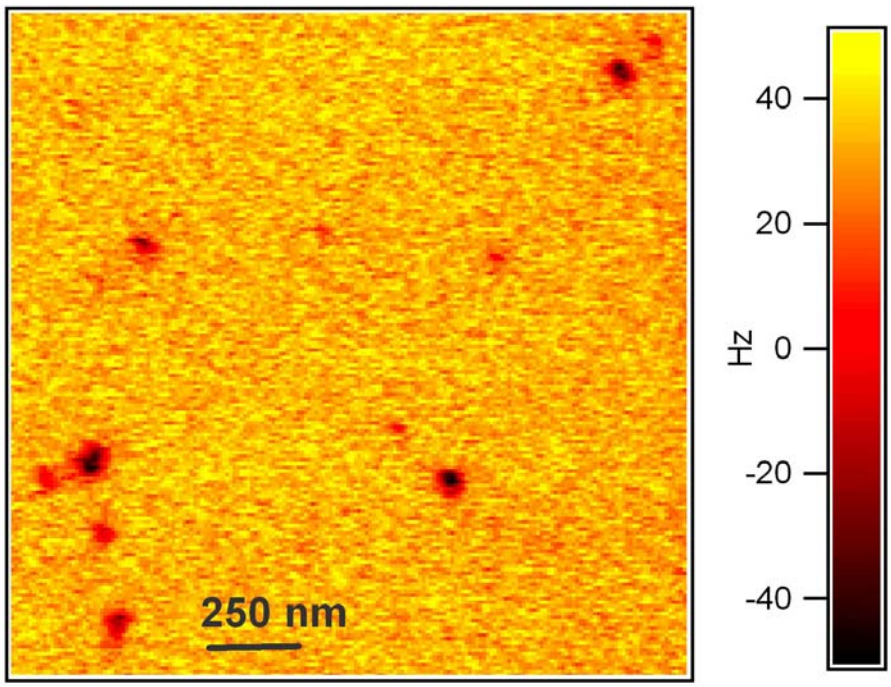

Figure 15. Charge image of CN-PPV nanoparticles deposited on clean glass substrate acquired using EFM. The shift in cantilever frequency is a function of the charge on the nanoparticle. The dark regions denote net negative charge on the nanoparticles and frequency shift indicates nominal excess charge of 2-8 electrons.

from the number and nature of charge carriers on the polymer chain. A negative shift in the cantilever resonance frequency due to charge interactions indicates, in this case, a net negative charge on the nanoparticle. This negative charge was generated during the ejection of the droplet from the orifice where the excess charges remain on the particle after solvent evaporation. Thus it was concluded that the particle orientation was a result of an interaction with the non protonated SiO^- groups on the glass surface. Modifications methods resulting in the removal of the negative charges (treating the surface with acid solution or silylation of the surface) from the substrate surface were found *not* to support polymer nanoparticle orientation. Table 1 shows the contact angle measurements carried out on differently treated coverglass surfaces. Only untreated coverglass was found to support orientation of the polymer nanostructures. Thus, it was found that the orientation was extremely sensitive to surface energy of the substrate. Molecular dynamics simulations predict the localization of charges on the surface of the polymer chain, isolated from the emissive species, which was believed to be buried inside a large number of chromophores.

Table 1: Contact angles of coverglass surfaces treated with different chemicals. The difference in the surface energies is believed to stem from different surface charge densities.

Type of treatment	Nature of nanoparticle orientation	Static contact angle (water)
Uncleaned (pre-cleaned by manufacturer)	**z-oriented**	**30°**
Base treatment	**In-plane oriented**	**24°**
Acid treatment	**In-plane oriented**	**12°**
Silanated	**In-plane oriented**	**99°**

3.4 Polarization Anisotropy Measurement

While the combination of images and AFM were consistent with a picture of folded, ordered geometries, they do not themselves provide proof of structure. Earlier work by Barbara et al.,[20] showed that excitation polarization anisotropy can be used as an effective tool to extract information about the structure of single conjugated polymer molecules. Since optically produced electron-hole pairs may be generated in any conjugated segment within a polymer, the organization of the chromophores within a single polymer chain will be manifest in excitation polarization anisotropy. The idea is that irrespective of the emissive site(s), all parts of the polymer can participate in absorption. Thus depending on the molecular conformation different luminescence response will be seen for polarization modulated input thereby yielding insights into the organization of the conjugated segments in a polymer chain.

Figure 16 shows how the organization of chromophores in a polymer chain is reflected in intensity distribution at different input polarizations. The observed luminescence intensity, $I(\theta)$, is a function of the rotation of the input polarization (θ) and the orientation of maximum absorption of the polymer chain (ϕ). Barbara et al.[20] modulated the polarization in the x-y plane (plane of the substrate) as the molecules were predominantly lying in the x-y plane. Thus a polymer random coil conformation will give little or no polarization anisotropy (M). A highly ordered polymer chain will have high polarization anisotropy. Thus an anisotropy parameter of ~0 indicates lack of intra-molecular order and a value close to 1 indicates a highly ordered polymer chain, where the conjugated segments are well aligned in one direction.

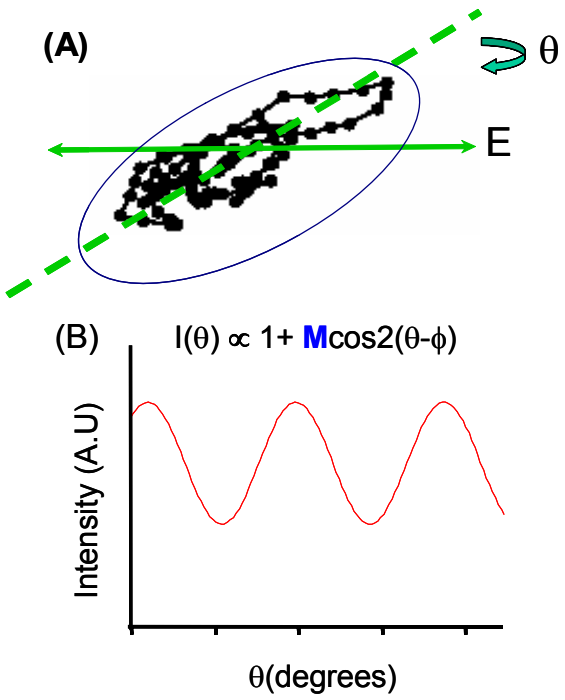

Figure 16. Schematic of the principle of excitation polarization anisotropy**.** The dashed line denotes the major axis of the absorption ellipsoid. E represents the electric field. θ is the angle of input polarization and ϕ is the angle of maximum absorption of the polymer chain

To make analogous polarization anisotropy measurements on the *z*-oriented samples, we modulated the *z*-component of the evanescent excitation field at the air-coverglass interface by rotating between *S* (transverse electric) and *P* (transverse magnetic) input polarizations with a half-wave plate. The *S* polarization has electric field components in the x and y and *P* polarization has electric field components in the z and y directions. These observations were performed through defocused illumination through the microscope objective, for which the effective excitation numerical aperture is quite low, thereby avoiding polarization scrambling characteristic of high NA optical systems. Multiple *P*-*S* rotations were made during individual nanoparticle measurements where we obtained polarization anisotropy parameters,

$$M = \frac{[I_P - I_S]}{[I_P + I_S]} \qquad (1)$$

Where, I_P and I_S are the spatially integrated fluorescence intensities for the two input polarizations for each complete rotation cycle. Control measurements on dye-doped polymer nanospheres (Molecular Probes) indicate negligible intensity bias between the two input polarizations. Figure 17 shows a representative polarization-modulated fluorescence intensity trace for an isolated *z*-oriented MEH-PPV nanoparticle compared with a background reference. In this particular example, the frame-averaged polarization modulation parameters were 0.88, 0.89, and 0.84 (±0.04) for the three *P*-S rotation cycles.

The known orientation of the emission moment, μ_{em}, for a given nanoparticle (from a fitting of the spatial fluorescence intensity patterns) allowed us to compare the measured fluorescence polarization anisotropy with geometrical approximations in some

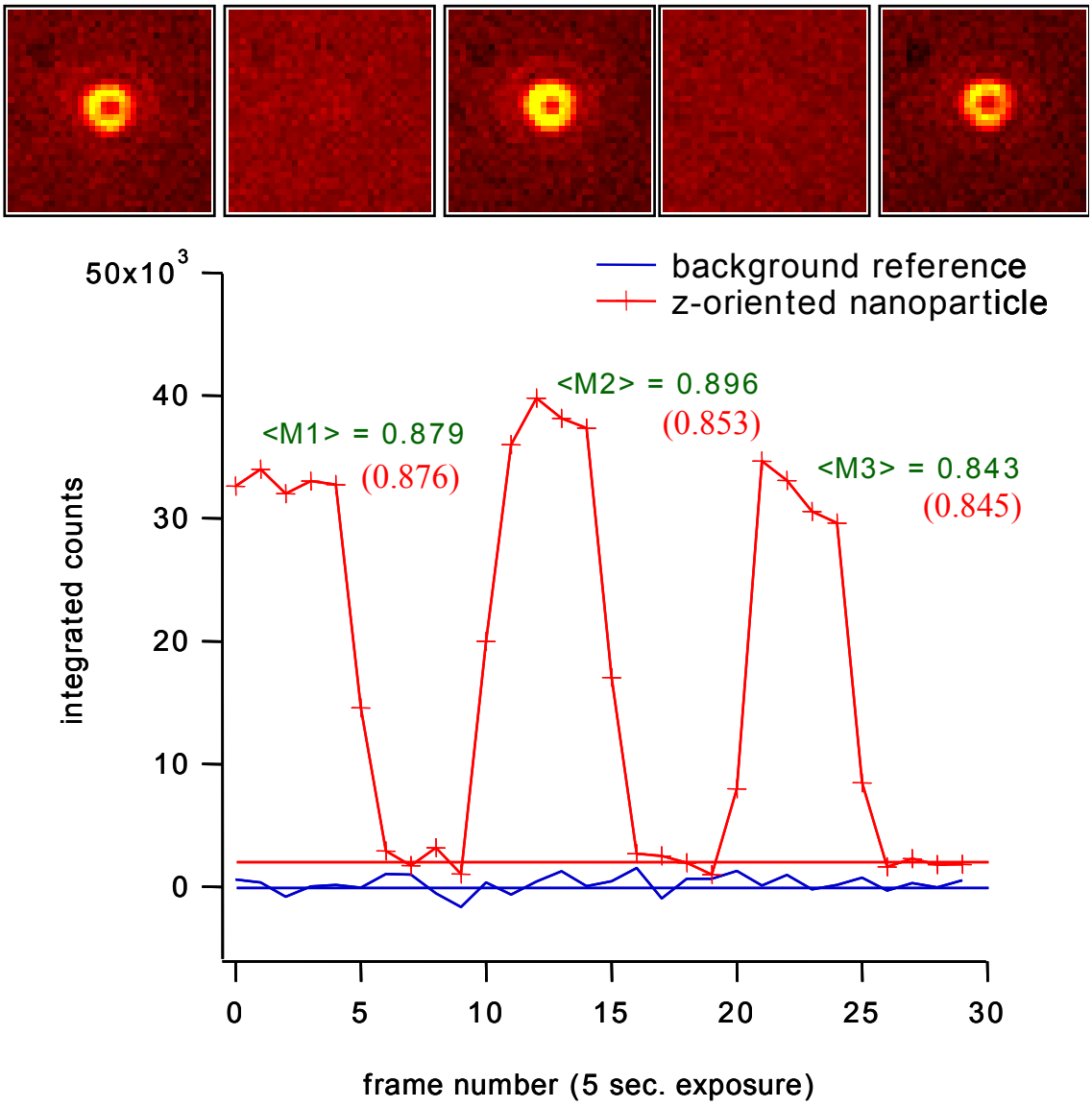

Figure 17. Fluorescence image under alternating P and S polarization of the excitation laser (top) and the corresponding intensity transients (bottom). The numbers red is the anisotropy parameters calculated by fitting the images and the numbers in green is the experimental value.

limiting cases to obtain further insight into nanoparticle structural organization. In these measurements, the polarization modulation in fluorescence intensity is a function of two components: (1) the structural organization within a given nanoparticle, which determines the depth of modulation and (2) the projection of the absorption moment, μ_{abs}, in the *x-y* plane. If $\mu_{abs} \approx \mu_{em}$, then the apparent excitation polarization anisotropy associated with the projection in the x-y plane can be estimated by

$$M_\theta = \frac{[\cos\theta - \sin\theta]}{[\cos\theta + \sin\theta]} \qquad (2)$$

where θ is the angle formed between μ_{em} and the surface normal, as precisely determined from emission pattern fitting. In the case where the tilt angle of μ_{abs} is significantly less than μ_{em}, M_θ will be lower than the measured value whereas the converse is true for the opposite case. We find that the measured M and M_θ are in excellent agreement, suggesting that μ_{abs} and μ_{em} are approximately collinear and that there is essentially no structural contribution to the in-plane component of the absorption moment.

Additional evidence for highly ordered intra-molecular structures was given by the histogram of anisotropy parameters compared with approximations of simulated distributions for different single-molecule morphological families (as well as experimental thin-film results) from ref 20. Figure18 shows a histogram of polarization anisotropy parameters from 260 z-oriented molecules, constructed and compared against the value reported in ref 20. Our experimental histogram on the *z*-oriented samples differs significantly in peak value from the simulation of rod-shaped (cylindrical) molecules (0.92 vs 0.7). The origin of this difference may probably be due to the fact that simulation parameters used in the bead-spring model by Barbara and coworkers[20] were unrealistic

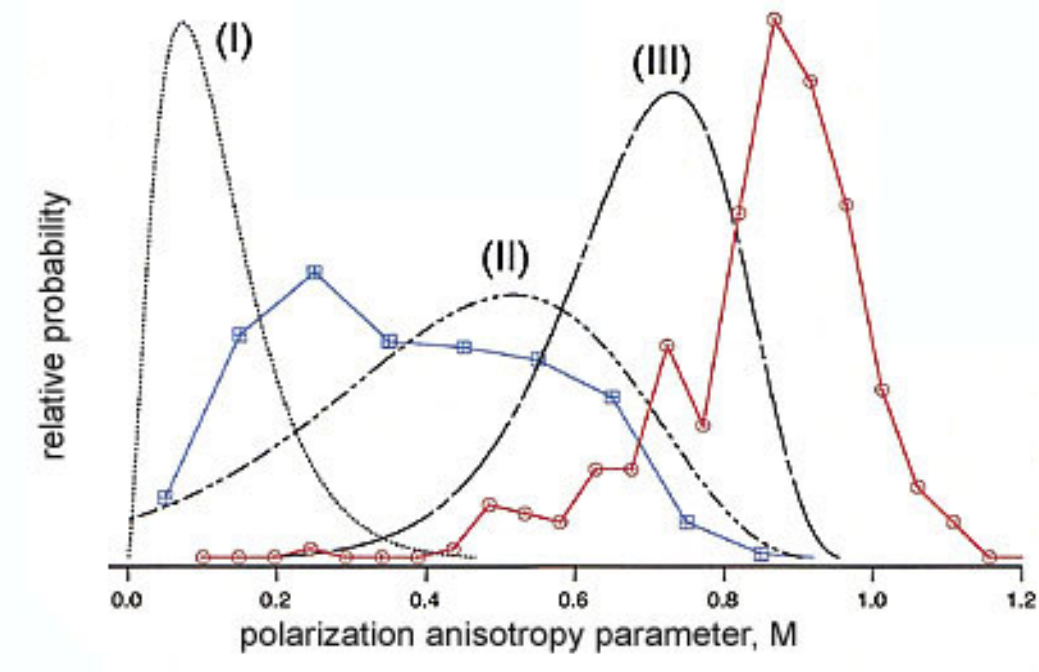

Figure 18. Combined anisotropy parameter (M) of more than 120 MEH-PPV nanoparticles from different samples (red lines and points) compared with thin film results (blue line and markers) and approximations of simulated distributions from ref. 20 for random coil (I), defect cylinder (II) and rod (III) intra-molecular geometries. Control measurements carried out on dye doped nile red nanoparticles, yielded M parameters similar to (I), indicating negligible bias in excitation intensity for two input polarizations.

(2.5 monomers/chromophore) compared with 10 monomers/chromophore in real polymers and tetrahedral defects in the polymer chains were not taken into account in the model. The observation of toroidal fluorescence emission patterns combined with AFM measurements and polarization anisotropy measurements strongly indicate that single MEH-PPV molecules were collapsed and oriented perpendicular to the substrate when prepared using microdroplet techniques.

3.5 Summary

In this chapter we have shown that single molecules MEH-PPV and CN-PPV prepared using droplet generator or nebulization can be oriented on glass coverslips. The observed fluorescence images were characteristic of z-oriented transition moments of the polymer molecules. The asymmetry in the emission pattern was used to calculate the tilt angle of the dipole with respect to the surface normal. The average tilt angle was found to be less than 5° to the surface normal. This observation of uniformly oriented transition dipoles pointed towards a collapsed polymer structure which was supported by AFM measurements on the oriented samples. The histogram maxima of particle height distributions for MEH-PPV and CN-PPV were found to be 8 nm and 10.6 nm respectively. These values fall within the range of the persistence length of soluble PPV polymers[5], consistent with a picture that the individual polymer molecules as folded oriented nanostructures. Structural information on oriented polymer molecules was obtained by excitation polarization anisotropy measurements. The histogram peak of polarization anisotropy parameter was found to be 0.92, indicating high internal structural order within individual polymer particles. This means that individual chromophores

within the molecules were organized approximately parallel to each other. It was believed that the polymer chains were folded at tetrahedral defects found in the polymer backbone. These experimental results were further supported by results obtained by hybrid molecular mechanics simulations. The molecular mechanics simulations also support our picture of collapsed, rod like polymer nanostructures with long axes oriented perpendicular to the substrate. The orientation mechanism of the molecules was found to be electrostatic in nature. EFM measurements carried out on nebulized CN-PPV molecules indicated that the molecules carried net negative charge. Surface modification of the glass coverslips resulted in-plane oriented polymer molecules. Contact angle measurements carried out on differently modified coverglass surfaces indicate that polymer orientation is highly sensitive to the nature of the substrate.

During the sample preparation steps it was observed that the chain collapse and orientation was strongly dependent on the choice of solvent from which the nanoparticle was prepared. Collapsed solution phase polymer chain conformations favored z-orientation of the polymer nanostructure[44]. To study the effect of solvent on the formation of dry polymer nanostructures the hydrodynamic radii of MEH-PPV and CN-PPV in various solvents were measured. Since the polymers under investigation were inherently fluorescent, fluorescence correlation spectroscopy (FCS) was used to measure the solution phase polymer chain conformations[44]. A detailed description of the technique and results are given in chapter 5.

CHAPTER 4

Spectral and Photophysical Properties of z-oriented Polymer Nanostructures

In the previous chapter we have established the structure of z-oriented polymer nanostructures, where the conjugated segments are organized nearly collinear to each other within a molecule with the long axis oriented perpendicular to the glass substrate. In this chapter the spectral and luminescence properties of z-oriented polymer nanostructures will be discussed in detail which will yield further information about the nature of the emissive site in z-oriented nanostructures.

The spectral and luminescence characteristics of z-oriented polymer nanostructures are markedly different from the in-plane oriented species or bulk polymer. The photochemical stability of z-oriented molecules in ambient conditions was found to be orders of magnitude higher than the in-plane oriented species under similar pump intensities. The fluorescence quantum efficiency of z-oriented nanostructure was close to unity and the excited state lifetime was nearly double that of in-plane oriented species. The fluorescence spectra of z-oriented molecules exhibited red shifted emission with considerably narrower full-width at half-maximum (fwhm) compared to the bulk polymer[44,45]. The emission maximum of individual molecules varied from particle to particle, but was red shifted with respect to the bulk. A histogram of the center frequency distribution of several z-oriented MEH-PPV nanoparticles revealed discretely quantized emission that was interpreted as discrete transition energies with well defined effective chromophore length. This indicates that emission takes place from a local radiative trap

state, which is not necessarily the longest conjugated segment. The incontrovertible evidence of single site emission comes from photon anti-bunching observed in z-oriented polymer nanostructures[45,46].

4.1 Photochemical Stability of z-oriented Polymer Nanostructures

Photochemical stabilities of single molecules of conjugated polymers are low in the presence of oxygen at ambient conditions. To enhance the photostability, typically conjugated polymers are embedded in a thin film of a polymer matrix[18,19,30]. However, the use of a supporting matrix may affect the photophysical properties of single molecules due to the interactions with the surrounding dielectric medium. To avoid host-polymer interactions, we carried out our experiments in the presence of oxygen at ambient conditions without a supporting medium. The photochemical stability of polymers in thin film environment is extremely low (typically a few seconds). Figure 19 shows the intensity transients of a z-oriented (A) and an in-plane (B) oriented CN-PPV single molecule under ambient conditions. It can be noted that the photochemical stability of z-oriented nanostructure is orders of magnitude higher than the in-plane oriented molecule. The difference in stability can be explained mainly in terms of the lower sample-substrate interaction for z-oriented nanostructure compared to the in-plane species. The chromophores of the in-plane oriented molecules are directly in contact with the substrate while the z-oriented molecule has minimum contact with the substrate by virtue of its orientation. In addition, the high structural order within the z-oriented molecule may offer higher relative protection of the emissive site from oxygen, compared to in-plane species.

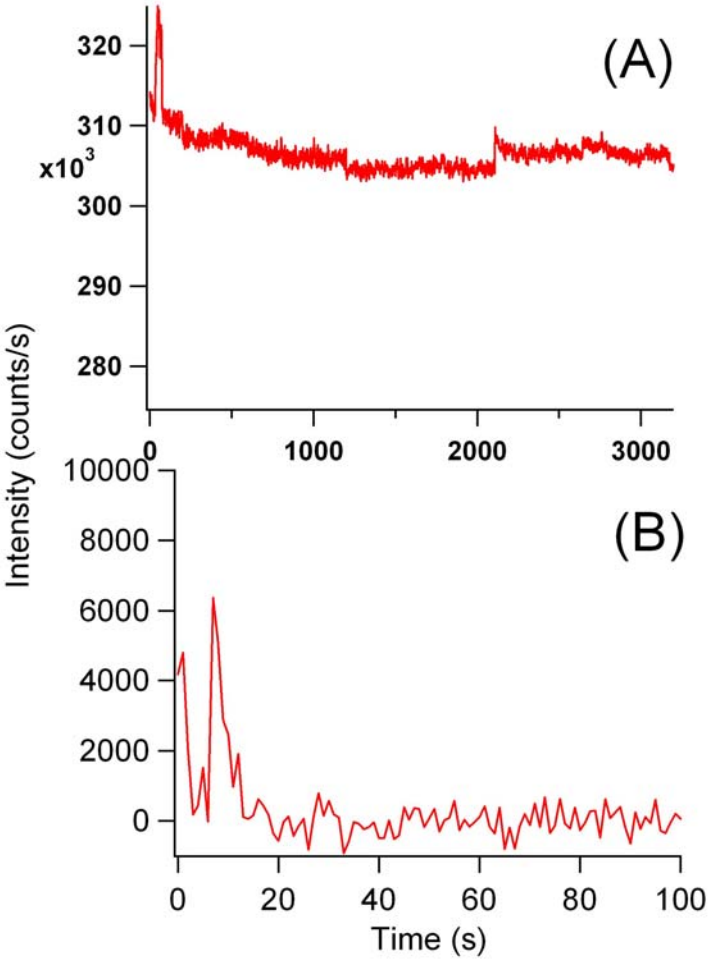

Figure 19. Fluorescence intensity transients of (A) a z-oriented molecule (B) and an in-plane (the substrate plane) oriented CN-PPV molecule acquired at ambient conditions. Note that the fluorescence signal from z-oriented particle represented in (B) persists for >30x, with count rates greater than 50x that of the in-plane species.

More detailed photophysical information on z-oriented species was obtained from examination of the photon counting statistics. For a single chromophore, the probability of measuring n photons prior to photobleaching is given by $P(n) = N \cdot \exp(-n \cdot \Phi)$ where $\exp(-\Phi)$ is known as the photobleaching quantum yield, or the probability per excitation cycle that photobleaching will occur. The exponential photoncount statistics for a single-chromophore simply reflect the Poisson (random) nature of the photochemical destruction process. For multi-chromophoric systems (that are uncorrelated), this distribution is expected to take the form of an *N*th-order convolution of exponentials where N is the number of independent chromophores. To compare the photochemical stability of z-oriented molecules with other materials (cadmium selenide, CdSe, quantum dot; DiI, organic dye), photobleaching quantum yield was calculated from experimental values. To calculate the photobleaching quantum yield, the species of interest was illuminated by argon ion laser and fluorescence image was acquired until photobleaching occurred. A histogram of total fluorescence counts of different species was constructed and curve-fitted to an exponential decay function. Table 2 compares the ϕ values for CN-PPV, MEH-PPV, DiI and CdSe. From Table 2 it can be seen that the CN-PPV is 2x times more stable than MEH-PPV which in turn is more stable than DiI which in turn is better than CdSe. This shows that z-oriented polymer nanostructures are better than CdSe in terms of photobleaching quantum yield. In addition, the advantages of CN-PPV and MEH-PPV over CdSe are easy sample production, commercial availability, and high photon count rates.

Table 2: Comparison of photobleaching quantum yields under ambient conditions.

Fluorescent molecule	**Photobleaching quantum yield**
Z-oriented CN-PPV	5.7×10^{-7}
Z-oriented MEH-PPV	1.06×10^{-6}
DiI(18)	5.4×10^{-5}
Cadmium Selenide	1.96×10^{-4}

4.2 Photoluminescence Spectra of MEH-PPV and CN-PPV

The photoluminescence (PL) spectra of z-oriented MEH-PPV and CN-PPV profoundly differ from the bulk polymer. Figure 20 shows a comparison of PL spectra of (A) a bulk sample of MEH-PPV and (B) a z-oriented molecule. The full width at half maximum (fwhm) of the PL spectra of the bulk polymer in Figure 21 is ~45 nm, while that of the single molecule is ≈20 nm, indicating narrow bandwidth emission from z-oriented polymer nanostructures. Figure 21 is a comparison of PL emission spectra of z-oriented and bulk CN-PPV molecule. In both MEH-PPV and CN-PPV, spectral narrowing of ≈20 nm (~0.1 eV) was observed in z-oriented nanoparticles compared to the bulk polymer spectra. Similar spectral narrowing was observed in highly ordered PPV samples prepared by in-situ polymerization by Friend and coworkers[47]. The spectral narrowing in z-oriented nanostructures is attributed to the structural order in the polymer nanoparticle.

Barbara and coworkers[18] have previously studied the luminescent trap states in MEH-PPV single molecules and observed multiple trap states with a low lying state where excitonic energy was 'funneled' to a low lying trap state. In the case of z-oriented single molecules only one luminescent trap state was accessed. No spectral diffusion was observed in the case of z-oriented nanoparticles, indicating a single emissive site. Infact spectral stability on the orders of hours was observed. The fluorescence emissions from z-oriented nanostructures were red shifted with respect to the bulk polymer. The amount of red shift varied from particle to particle. The origin of the red shift is believed to be due to the self-solvation of chromophores. The ordered structure of the z-oriented

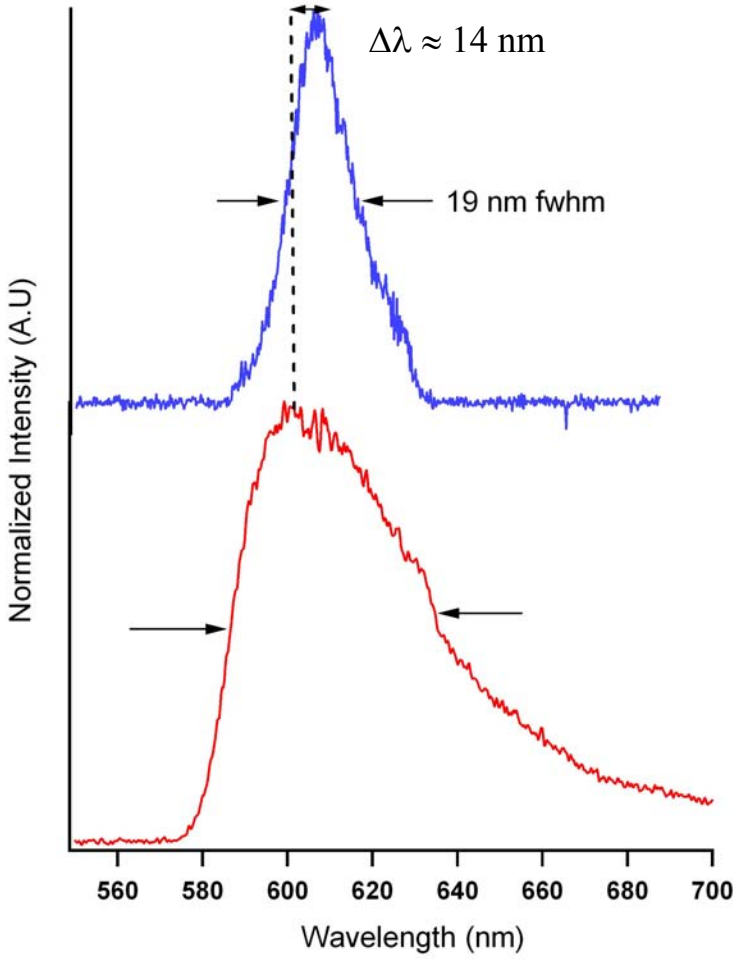

Figure 20. Fluorescence emission spectra of a z-oriented MEH-PPV single molecule (top) and a bulk sample of MEH-PPV (bottom). Spectral narrowing is observed in the case of oriented single molecule (19nm fwhm) compared to the spectra of the bulk sample (45nm fwhm). A red shift of 25 nm (>0.1 ev) in peak photoluminescence emission is also observed for the z-oriented single molecule compared to the bulk.

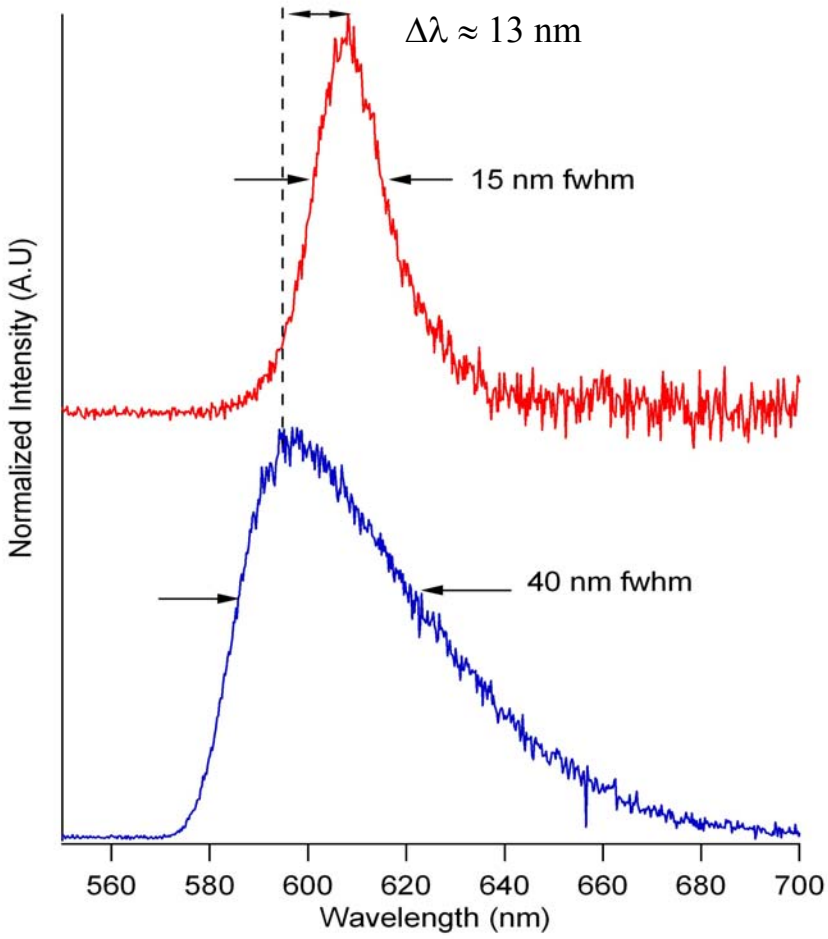

Figure 21. Fluorescence emission spectra of a z-oriented CNPPV single molecule (top) and a bulk sample of CNPPV (bottom). Spectral narrowing is observed in the case of oriented single molecule (15nm fwhm) compared to the spectra of the bulk sample (40nm fwhm). A red shift of 20 nm (0.1 ev) in peak photoluminescence emission is also observed for the z-oriented single molecule compared to the bulk.

polymer increases the π-π overlap between the chromophores which in turn shifts the emission to the longer wavelength due to a lowering of energy of the luminescence trap state.

In contrast with bulk or in-plane single-molecule spectra, which closely resemble molecular dye fluorescence, *z*-oriented nanoparticle spectra show only a *single* narrow peak with line widths ranging from 10 to 15 nm fwhm. The line shapes are approximately Gaussian, and many individual particle spectra show some weak vibronic structure (Figure 20) as well. Similar spectral narrowing was observed by Friend and co-workers[30] in highly ordered macroscopic PPV samples prepared by in situ polymerization. This observation provides an interesting contrast with spectral measurements made previously by Barbara and co-workers. In their experiments, different luminescent trap states were evidenced by comparing single-molecule emission spectra at successive times during illumination with a range of accessible energies observable through spectral subtraction[18]. In our case, only a *single* emissive state is accessed for the entire photochemical lifetime of the molecule. In following the spectral dynamics on a time scale of 5 frames per second, we found that there is essentially no spectral diffusion and that the emission center frequency is fixed-but *different*-for each particle.

Figure 22 shows a histogram of the peak wavelengths obtained from >350 individual nanoparticles. We see two clearly defined sharp peaks in the distribution at 608 and 613 nm with less well-defined components at 598.5 and 618 nm. The energy difference between these peaks in the center frequency distribution is in reasonable agreement with zero-order electronic energy differences between conjugation lengths, *L*,

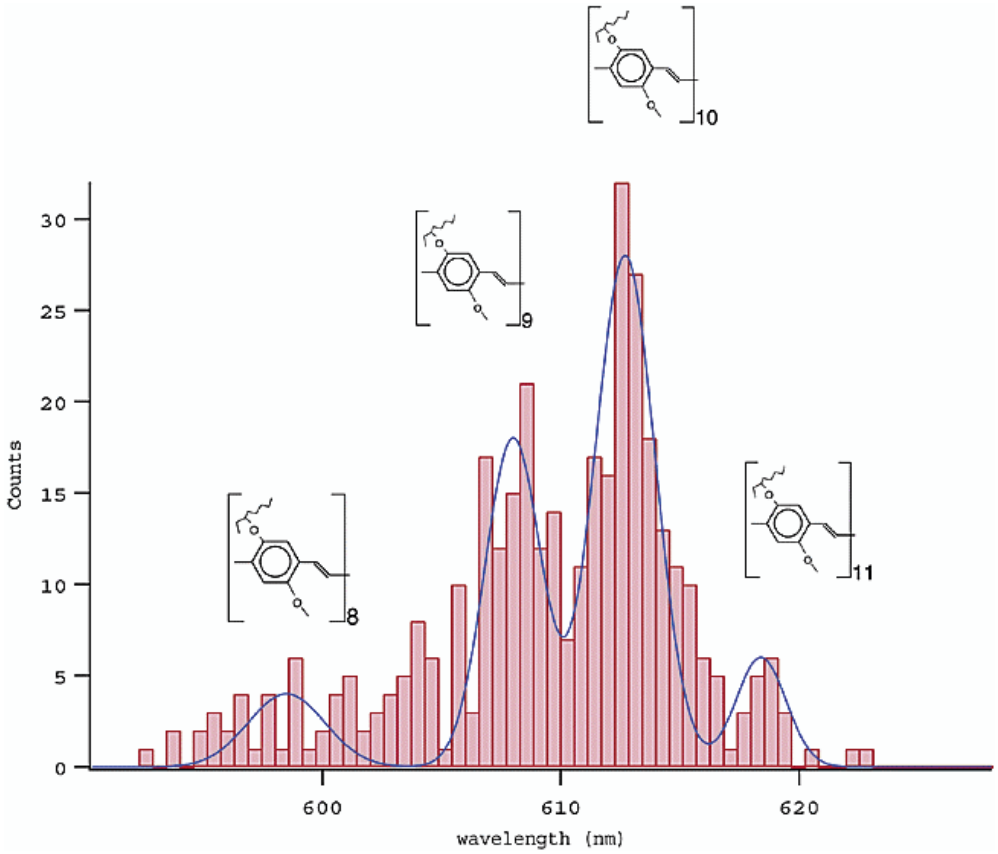

Figure 22. Histogram of center frequencies from emission spectra of *z*-oriented MEH-PPV nanoparticles (sample size =380, bin width= 0.5 nm). The blue curve is a model function that is a sum of four Gaussian components with peak wavelengths of 598.5, 608, 612.7, and 618.5 nm. These peaks are correlated with zero-order electronic energies for conjugated segments composed of 8, 9, 10, and 11 monomer units taken from ref 16 and indicated with the inset graphic.

of 8, 9, and 10 monomer units ($\Delta_{8\text{-}9}$ = 200 cm^{-1}, $\Delta_{9\text{-}10}$ = 149 cm^{-1} $\Delta_{10\text{-}11}$ = 115 cm^{-1}) calculated from $E(L) = E_0 + 2\beta \cos(\pi L/(L + 1))$, where E_0 = 34 400 cm^{-1} and β= -8800 $cm^{-1.}$ where E_0 is the energy of the excited state and β is the interaction strength between nearest neighboring units[48]. In terms of absolute energies, the measured data indicate lower energies (compared unfolded chain) per chain of 1150 cm^{-1}, which presumably derive from a lowest unoccupied molecular orbital (LUMO) lowering of the emissive chromophore by virtue of aligned conjugated segments within the core of the nanoparticle.

Even though every MEH-PPV molecule should be reasonably expected to contain a distribution of conjugated segment lengths, a single particle displays a spectrum characteristic of only *one* of them, which does not necessarily correspond to the lowest (vacuum) energy state available within the particle. In other words, why does a given particle emit with a frequency characteristic of, say, L = 9 frequency when it presumably has access to longer conjugation lengths. In a picture of exciton funneling to particular luminescent trap states described by Barbara and co-workers[18], a dipole-dipole energy transfer process would seem to predict only a single peak in the center frequency distribution corresponding to the lowest singlet-exciton energy accessible within the particle. While the statistics for the PLE center frequency histogram peaks nominally at 598.5 and 618 nm are obviously not as clear as those for the two main peaks, there is a clear correlation of the cluster of these measurements with the oligomer S_1-S_0 transition energies.

We believe that the discrete distribution of center frequencies observed in photoluminescence from *z*-oriented MEH-PPV nanoparticles reflects (1) the distribution of conjugated segment lengths, (2) coupling between segments within the particle, and (3) the structural arrangement within each macromolecule/nanoparticle. In the case of a highly axially aligned chain structure, one should expect significant LUMO energy lowering for conjugated segments in the core of the particle due to favorable self-solvation effects on the protected, emissive chromophore. The extremes in solvation between vacuum on the outside of the nanoparticle and aligned MEH-PPV chains on the inside would lead to even more significant lowering of the HOMO-LUMO gap for any species in the particle interior. This solvatochromic shift is much larger than the spread in HOMO-LUMO energy of different MEH-PPV chromophore conjugation lengths. Thus, depending on the structural details of each individual nanoparticle, the lowest LUMO state is always accessed with its corresponding emission frequency. As indicated by the observed distribution of nanoparticle emission center frequencies, this does not necessarily correspond to the longest conjugated segment but instead to the chromophore with the lowest energy emission due to favorable solvation effects. This means that if the distribution of conjugated chain lengths could be precisely controlled, oriented nanoparticles with a single frequency could be prepared.

4.3 Fluorescence Lifetimes and Quantum Yields of CN-PPV Nanostructures

The quantum efficiency of CN-PPV nanostructures was measured relative to DiI in PMMA. Brus and coworkers have established near unity quantum yield for this system

and thus provide a good reference. In order to make the measurement, the luminescence spectra of the molecules were taken under same laser illumination intensity. The total area under the curve/total area for DiI gives the reference for the quantum yield. We also measured the fluorescence lifetime of CN-PPV molecules. The fluorescence quantum yield and fluorescence lifetimes was measured for in-plane oriented CN-PPV in PMMA and z-oriented CN-PPV. The fluorescence quantum yield and fluorescence lifetime is related through equation 3.

$$\Phi = 1 - \frac{\tau}{\tau_{nr}} \tag{3}$$

Where, Φ is the fluorescence quantum yield, τ is the fluorescence lifetime, τ_{nr} is the non-radiative component of fluorescence lifetime. The fluorescence lifetime is related to the radiative and non-radiative lifetimes through Equation 4.Where, τ_r is the radiative

$$\frac{1}{\tau} = \frac{1}{\tau_{nr}} + \frac{1}{\tau_r} = \Gamma_{nr} + \Gamma_r \tag{4}$$

component Γ_{nr} and Γ_r are the non-radiative and radiative decay rate respectively. From the measured values of Φ and τ, both τ_{nr} and τ_r can be determined. Figure 23 shows the fluorescence decay of CN-PPV in three different conditions: (A) CN-PPV embedded in PMMA, (B) in-plane oriented and (C) z-oriented respectively. The experimental curves are fitted with exponential decay function to extract the fluorescence lifetime τ. Table 3 shows the values of Φ, τ, τ_{nr} and τ_r. The values of τ_{nr} and τ_r were calculated using

equations 3 and 4. The differences in the values in Table 3 can be explained in terms of the interaction of the emission dipole with a dielectric medium. Spontaneous emission from a source takes place due to the interaction of a dipole with the vacuum electromagnetic field[49]. Thus it is possible to modify the decay rate of a dipole by altering the vacuum electromagnetic field[50]. The vacuum electromagnetic field can be modified either by putting the dipole near a dielectric interface or by confining the dipole within a nanoscale dielectric. Placement of a dipole in a confined geometry alters the vacuum electromagnetic field due to reflections from the dielectric boundaries[51]. This alteration in the radiative decay rate depends on the orientation of the dipole and the distance between the dipole and the dielectric boundary[51]. Chew carried out theoretical calculations[52] on the change in radiative decay rate when a dipole is confined inside a nanoscopic sphere where the diameter of the sphere is much smaller than the emission wavelength[52]. Experimental verification of this phenomenon has been observed in many systems[53-55]. Sandoghdar and coworkers[49] have showed that radiative decay of europium ions can be modified by confining the ions in nanoscale silica spheres. Macklin et. al.[56] showed the effect of a dielectric interface and the dipole orientation on the radiative life time of carbocyanine (DiI) dye molecule.

The question we are interested here is the effect of orientation and nanoscale confinement of emission dipole in a dielectric medium. We wanted to quantify the change in the radiative lifetime of z-oriented CN-PPV molecules due to the presence of a dielectric interface and orientation and the confinement of the dipole within a nanoscale dielectric. To study both the effects we compared the radiative lifetimes of CN-PPV nanostructures in three different environments. Table 3 compares the lifetimes of

Table 3: Lifetimes and fluorescence quantum yield of CN-PPV.

	τ (measured)	**τ (non-radiative)**	**τ (radiative)**	**τ (orientation and Confinement effect)**	**Measured quantum yield (Φ)**
CN-PPV in PMMA	2.38 ns	4.11 ns	5.65 ns	5.65 ns*	0.421
In-plane CN-PPV	4.1 ns	5.77 ns	14.17 ns	16.9 ns†	0.300
Z-oriented CN-PPV	8.84 ns	982 ns	8.9 ns	9.4 ns‡	0.991

* Reference value, τ_r^{bulk}

† $\tau_r \approx 3 \times \tau_r^{bulk}$

‡ $\tau_r \approx (3 \times \tau_r^{bulk})/ 1.8$

CN-PPV dispersed in PMMA, oriented in the plane of the substrate and oriented perpendicular to the substrate. The three environments are illustrated schematically in Figure 23. The radiative lifetimes of the molecules in the three different cases can be compared by knowing the orientation of the dipole and the distance from the dielectric boundary.

For a dipole confined in a dielectric nanosphere, the decay rate Γ is given by equation 5[49].

$$\frac{\lim_{R\to 0}\Gamma_r}{\Gamma_r^{bulk}} = \frac{\tau_r^{bulk}}{\lim_{R\to 0}\tau_r} = \frac{9}{\left(n^2+2^2\right)n} \qquad (5)$$

Where τ_r is the radiative lifetime of the dipole located at a distance R from the interface, τ_r^{bulk} is the radiative lifetime of the dipole in a bulk medium and n is the refractive index of the dielectric. This often-termed "Rayleigh particle effect", results if the dipole is oriented at an angle θ with respect to the surface normal, the effect of orientation on the decay rate is given by equation 6[57].

Where a_1 and a_2 are parameters that describe variation of τ with respect θ and z is

$$\frac{\tau_r^{bulk}}{\tau_r} = \left[a_1(z)\sin^2(\theta) + a_2(z)\cos^2(\theta)\right] \qquad (6)$$

the distance of the dipole from the interface. The value of a_1 and a_2 depends on the dielectric interface and the location of the dipole; here $a_1(z) \approx a_2(0)$. The effect of dipole orientation is illustrated in Figure 24. Now the three cases given in Table 3 are analyzed

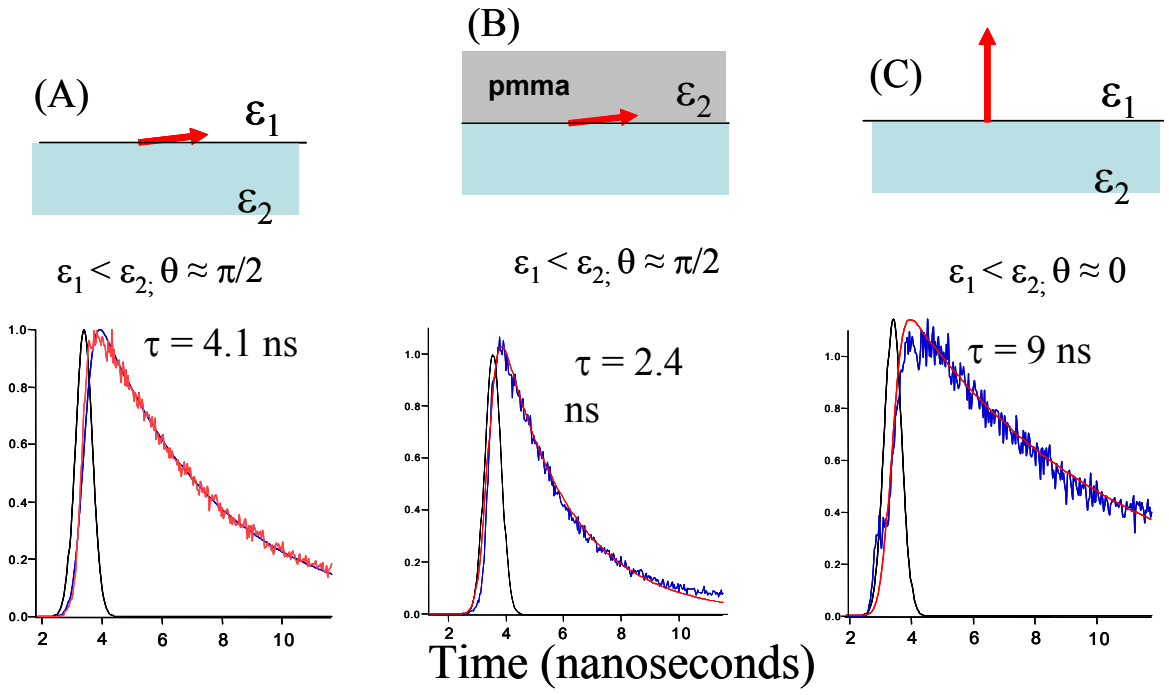

Figure 23. Measured fluorescence lifetimes of CN-PPV nanostructures in three different environments. (A) In-plane oriented CN-PPV, (B) CN-PPV embedded in PMMA and (C) z-oriented CN-PPV. ε is the dielectric constant. The y axis is normalized intensity in arbitrary units. The arrow represents the emission dipole of CN-PPV.

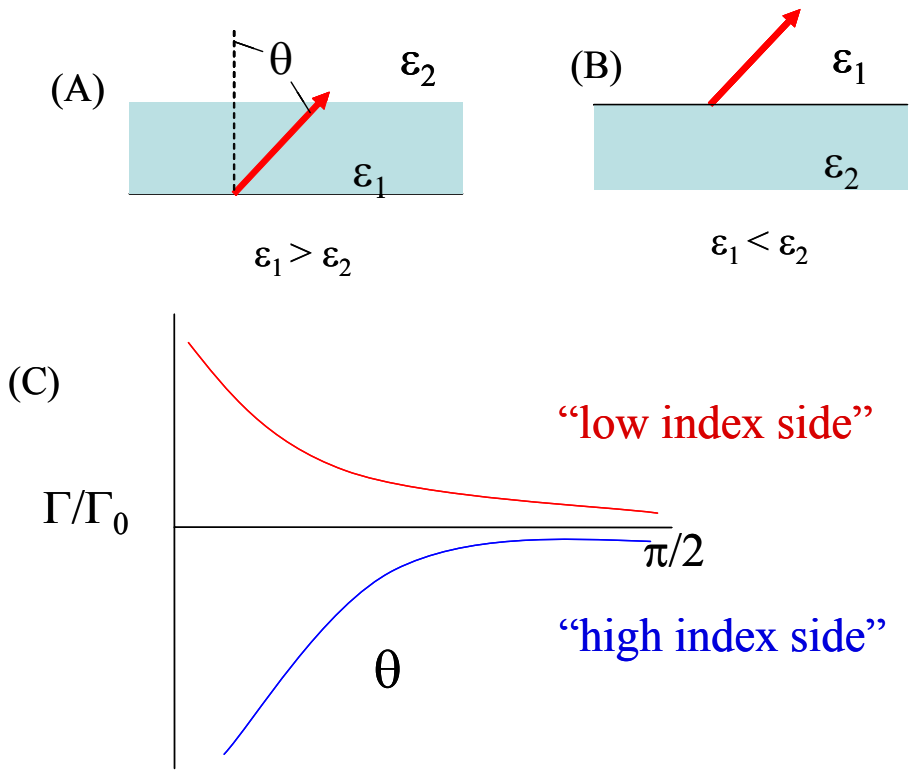

Figure 24. Schematic illustrating the effect of dipole orientation of a dielectric interface on the radiative decay rate with respect to the bulk value. Schematic (A) and (B) illustrates the location of a dipole on the high and low side of the dielectric interface. Plot (C) illustrates the change in the radiative decay rate with the orientation of the dipole with respect to the surface normal.

separately. For PMMA-air interface a_1 and a_2 are 0.92 and 1.6 respectively, when the dipole is located on the air side of the interface[56]. Thus for CN-PPV in PMMA the radiative lifetime (τ_r^{bulk}) is calculated as 5.65 ns using equations 3 and 4. The case of CN-PPV in PMMA can be approximated as a dipole in a dielectric medium where the dimensions of the dielectric are greater than the transition wavelength of the dipole. Hence the radiative lifetime is equal to that in a bulk medium.

For in-plane oriented CN-PPV the radiative lifetime was calculated (14.17 ns) from the measured values of fluorescence quantum yield and fluorescence lifetime. From our discussion in the last chapter we have surmised on the basis of photostability and spectral signatures that the emission dipole is perhaps, surrounded by conjugated segments in the polymer molecule. This can be roughly approximated to a case where the dipole is enclosed in a nanosphere (where the diameter of the nanosphere $d<<\lambda$, the emission wavelength, Figure 25). Thus by substituting for the refractive index of CN-PPV, n=1.5 and τ_r^{bulk}=5.65 ns in equation 3, we can see that $\tau_r \approx 3 \times \tau_r^{bulk} \approx 16.9$ ns, which is comparable to 14.17 ns within experimental error.

In the case of z-oriented nanostructure "Rayleigh particle effect" combined with orientation effect affects the lifetime of the particle. Thus by applying corrections using equations 5 and 6, we get $\tau_r \approx (3 \times \tau_r^{bulk})/1.8 \approx 9.4$ ns, which is comparable to 8.92 ns obtained from the measurements. Thus the radiative lifetime is decreased (instead of increase due to "Rayleigh particle effect) due to orientation effect.

The results from the three discussions above reinforce our belief that the emission dipole in the polymer nanostructure is surrounded by other conjugated segments

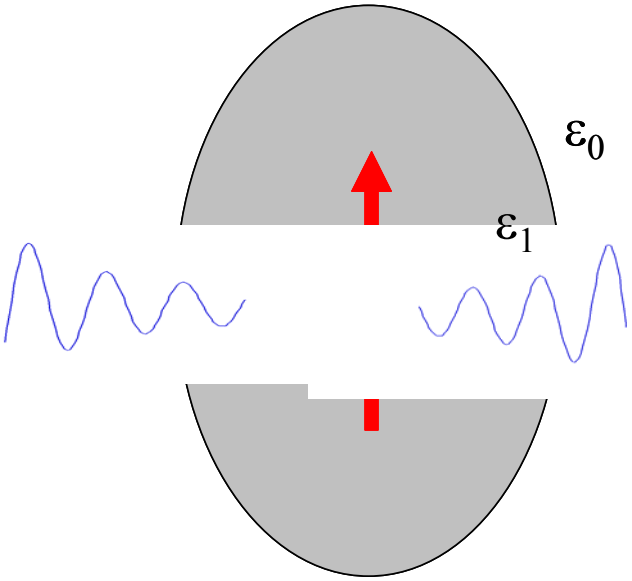

Figure 25. Illustration of a CN-PPV nanostructure. The red arrow is the emission dipole. The gray area surrounding the dipole is composed of conjugated segments in the polymer chain. Thus the scenario can be approximated as a dipole confined in a nanoscale dielectric. The refractive index ($n= (\varepsilon_1/\varepsilon_0)^{0.5}$) of CN-PPV is approximately 1.5 (≈refractive index of PMMA). ε_1 and ε_0 are the dielectric constants for CN-PPV and air respectively.

("Rayleigh particle" approximation). The results also stand as one of the experimental evidences of change in the radiative lifetime due to the effect of dipole orientation and dielectric confinement.

4.4 Photon Correlation Measurement

We have shown that the lifetime can be modeled as a dipole antenna under dielectric confinement. The combination of dipole emission patterns, narrow spectral signatures, and discrete photobleaching etc. all point to single chromophore emission from z-oriented polymer nanostructures. However, definitive evidence of single site emission from a z-oriented molecule comes from photon correlation measurement. The experiment is based on the concept that an ideal single quantum system should emit only a single photon/excitation. That is when a photon is emitted and detected at one detector; the probability of detecting another photon at the same time is zero. Thus a correlation of arrival times of photons between two orthogonal detectors can be established. The distribution of photon detection coincidences separated by a time interval τ is measured in the experiment. Photon correlation measurement was carried out on single molecules of CN-PPV using Hanbury Brown-Twiss[58] configuration (Figure 26). The correlation of the arrival times between two photons from a single polymer molecule was measured using this configuration. The second order correlation function $g^2(\tau)$, which is given by the following equation 7:

$$g^2(\tau) = 1 - (1/\ N)\exp\left[-(W_p + \Gamma_f)\tau\right] \qquad (7)$$

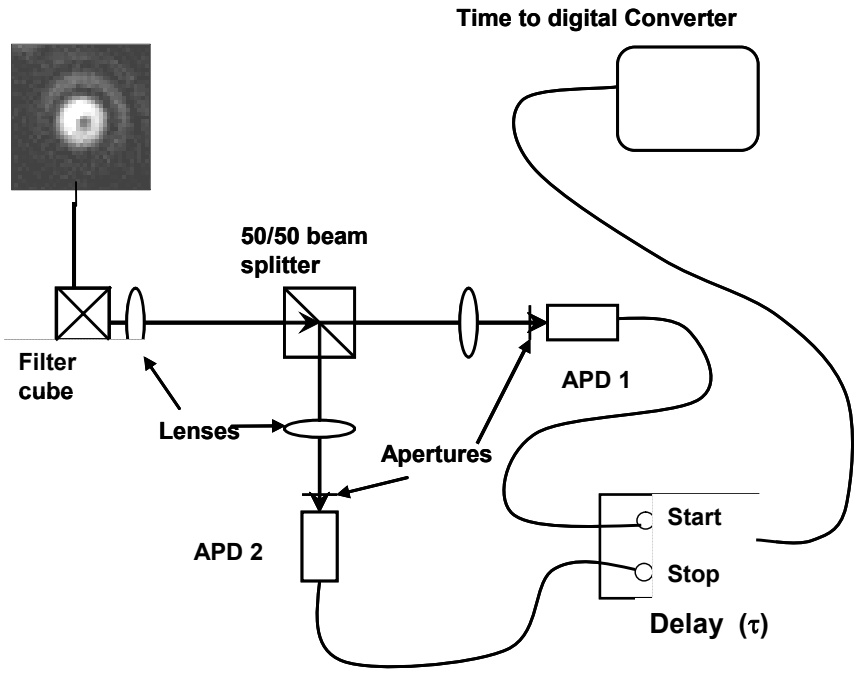

Figure 26. Schematic representing photon correlation measurement.

where, W_p is the pumping rate, Γ_f is the fluorescence decay rate, and N is the number of emissive sites within the polymer molecule. For large N, $g^2(\tau=0)$ approaches unity and the emitted radiation appears classical; for single quantum emitters (N=1) and $g^2(0)\approx 0$, and the phenomenon is known as photon anti-bunching[59]. If all the chromophores in one z-oriented polymer chain emit at the same time then $g^2(0)>>1$, and the phenomenon is known as photon bunching. Luminescence from a single CN-PPV nanostructure was isolated by translating the sample to locate the particle of interest on a target registered with a confocal aperture on the side port. The light was collimated through a 50/50 beam splitter and imaged onto two photon-counting avalanche photodiodes (APD, Perkin-Elmer SPCM-AQR-14, total instrument response time ≈600 ps). The time intervals between the APD detection events were measured with a PC based time to digital converter (TDC, Time Harp 200, PicoQuant Gmbh, 34 ps resolution). Typical laser (continuous wave, cw) pump intensity was ~5kW/cm^2.

Figure 27 shows typical $g^2(\tau)$ data from a single z-oriented CN-PPV nanostructure under cw Ar+ illumination at 514.5 nm and an intensity at the surface of ≈12 kW/cm^2. The total fluorescence count rate was 98 kHz, yielding a TDC count rate of ≈500 cps. The data shown in figure 27 was accumulated in 5 minutes. The solid curve shows $g^2(\tau)$ calculated using equation 7. The purity of the single-photon emission from the nanoparticle is reflected in the modulation depth of the signal at zero time delay ($g^2(\tau=0)$). However there are experimental factors which contribute to non-zero $g^2(0)$, as well. The condition that $\tau_{fluorescence} >> \tau_{instrument\ response}$ must be satisfied for $g^2(0)$ to have physical meaning. The small variation from zero is attributed to the finite instrument

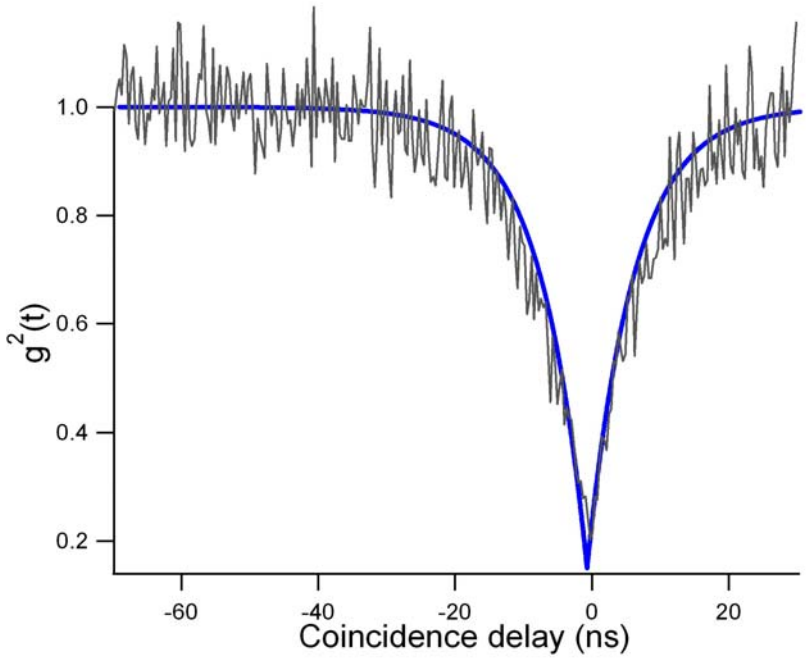

Figure 27. Measured $g^2(\tau)$ from a single z-oriented CN-PPV nanostructure with cw radiation (514.5 nm). Total fluorescence count rates were 98 kHz, with 10^5 time-to-digital conversion (at 34 ps resolution).

response of the system. The result was consistently reproducible with a modulation depth of 0.9±0.02 from particle to particle with very little effect on pump intensity. This observation of photon anti-bunching is incontrovertible evidence of local radiative recombination at a single site in z-oriented nanostructures. The result follows the conclusion reached in the previous section where the excitonic energy is funneled into a local chromophore within the highly ordered nanoparticle, where radiative recombination takes place.

High photostability, high fluorescence count rates and high purity single photon emission with high modulation depth (≈0.9) from single z-oriented nanostructures make them an interesting candidate for single photon sources in quantum cryptography applications competing favorably with nitrogen vacancy center and cadmium selenide. For such applications, photon-on-demand capability is critical. We measured $g^2(\tau)$ from individual *z*-oriented nanostructures using a mode-locked Ar+ laser (120 ps pulse width, 76 MHz repetition rate) to study the nature of emissive site at peak powers generated in a pulsed laser. Figure 28 shows measured $g^2(\tau)$ from a single particle excited with a mode-locked Ar+ laser with an average intensity of ≈10 kW/cm^2. In contrast with cw measurements, pulsed $g^2(\tau)$ measurements on systems where the fluorescence lifetime of the emitting species is short compared to the pulse period, the relatively long fluorescence lifetime 8.8 ns of the *z*-oriented polymer species results in overlap between adjacent peaks. For these data, we observe a value for $g^2(0)=0.15$, which is dominated from overlap of peaks at ±13 ns with respect to $\tau=0$.We find maximum measured

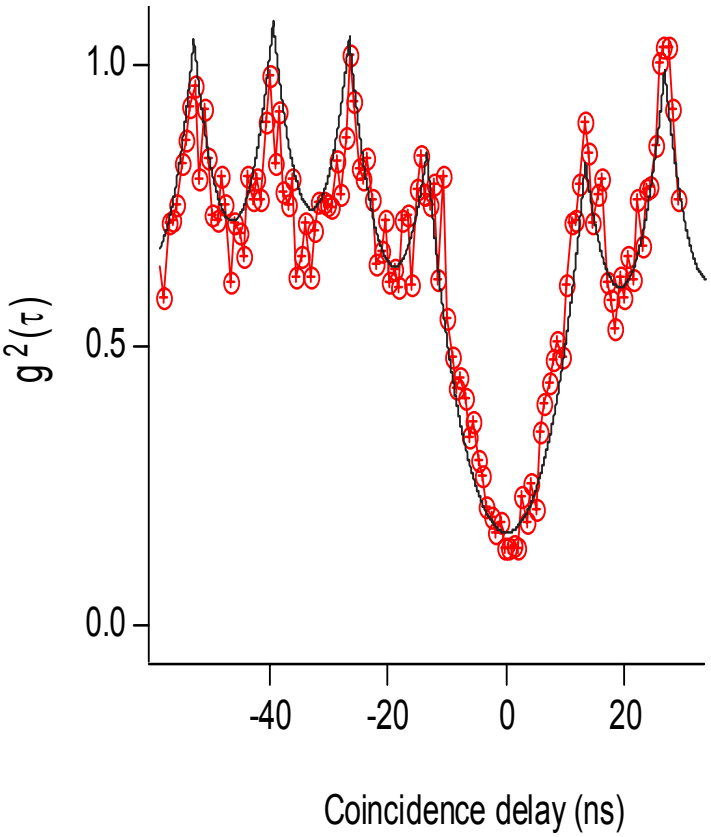

Figure 28. Measured $g^2(\tau)$ from a single z-oriented nanoparticle under mode-locked excitation (ω=75.55 MHz) with average intensity at the sample ≈10 kW/cm^2.

fluorescence count rates under modelocked excitation of about 60 kHz, corresponding to a per pulse fluorescence photon generation efficiency of ≈5%.

4.5 Summary

In this chapter we have discussed the luminescence and photophysical properties of MEH-PPV and CN-PPV. The fluorescence emission spectra of both z-oriented MEH-PPV and CN-PPV show red shifted emission with considerable spectral narrowing. Typically the spectral narrowing is on the order of ≈20 nm (0.1 eV) with respect to the spectra of the bulk polymer. The histogram of central frequency distributions of z-oriented MEH-PPV showed two distinct peaks along with two weak peaks. The peaks could be fit to multiple Gaussian components with peak wavelengths of 598.5, 608, 612.7, and 618.5 nm. These peaks can be correlated to zero-order electronic energies for conjugated segments with 8, 9, 10, and 11 repeating units. This point to efficient energy funneling between the chromophores where the absorbing chromophores transfer its excitonic energy to a local radiative trap site which can be composed of 8, 9, 10 or 11 repeating units. Thus the emissive site is not necessarily the longest chromophore, rather a conjugated segment whose HOMO-LUMO gap is lowered due to the self solvation of chromophores. Thus typically the emissive site is solvated by other conjugated segments and is buried inside a 'bundle' of conjugated segments. The z-orientation coupled with the structural order is believed to enhance the photostability of z-oriented nanostructures in comparison to the in-plane oriented molecules. The z-orientation reduces electronic perturbation from sample-substrate contact and thus reduces probability/excitation cycle of non-radiative decay, reflected in enhanced quantum yields. The picture of the emissive

site encased by other conjugated segments is confirmed from the fluorescence quantum yield and lifetime measurements.

The measured values of radiative lifetimes compare well with the calculated values for a dipole confined in a nanoscale dielectric (here conjugated segments of the polymer) and oriented perpendicular to the dielectric boundary. Final and incontrovertible evidence of single site emission in z-oriented nanostructures from photon correlations measurements carried out on z-oriented CN-PPV molecules.

CHAPTER 5

Effect of Solution Phase Chain Conformation on Chromophore Orientation

In this section, the effect of solvent and droplet on the collapse and orientation of polymer nanostructures will be discussed. During the preparation of polymer samples from different solvents, strong correlation was found between the choice of the solvent and the sample quality in terms of polymer nanoparticle orientation. Figure 29 A and B shows high-spatial resolution fluorescence images of CN-PPV prepared from toluene (relative polarity= 0.099) and DCM (relative polarity= 0.309), respectively for similar substrate, droplet size, rare-gas pressure, polymer concentration and sample collection time. Earlier, it was speculated that the effect of three-dimensional confinement in the micro-droplet played a dominant role in this self-organization. However under conditions of extremely rapid solvent evaporation (≤ 1 ms), the molecule will not have sufficient time to organize in response to the surface energy stress and will essentially become quenched in a configuration similar to its equilibrium solution-phase structure.

Samples with z-oriented molecules were conveniently prepared from toluene solution, while z-oriented species were *not* observed for polymer samples nebulized from dichloromethane (DCM) as shown in Figure 29 B. The fluorescence images of samples prepared from DCM appear mostly as simple diffraction-limited spots, while samples from toluene yield 'donut' like emission patterns indicative of z-oriented molecules. These results suggest that the difference in the emission patterns of CN-PPV (with

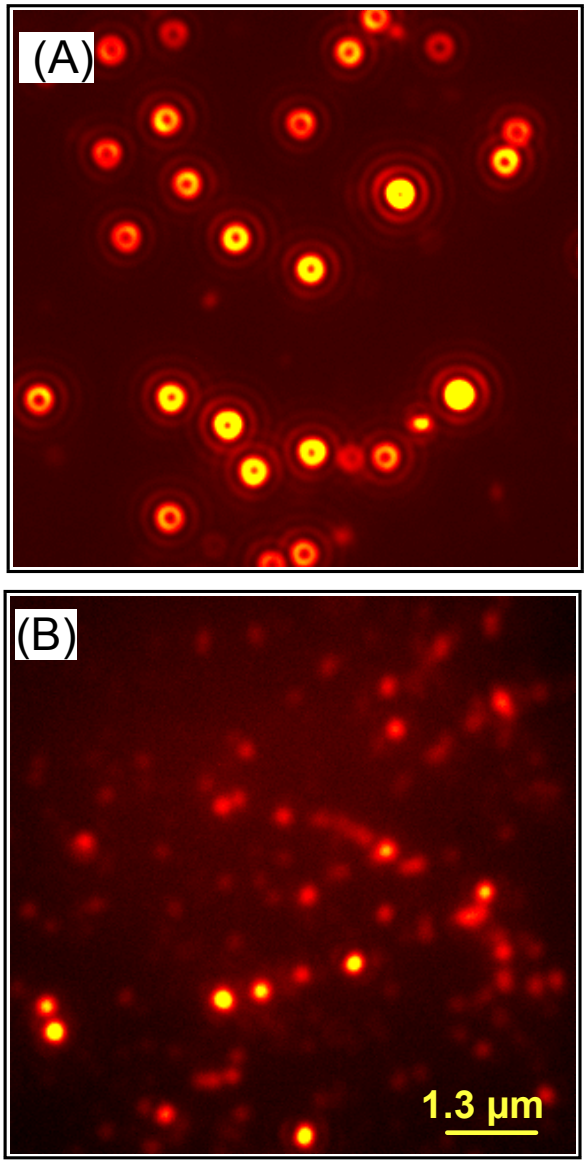

Figure 29. Fluorescence emission pattern images of CN-PPV single molecules prepared by nebulization from (A) Toluene and (B) dichloromethane solutions. The 'doughnut'-like patterns in (A) are indicative of single dipole emitters oriented perpendicular to the substrate. The in-focus diffraction limited spots in (B) are indicative of random orientation of dipoles with in single polymer molecules.

similar results observed for MEH-PPV) prepared from toluene and DCM was a direct consequence of the polymer chain conformation in the solution phase. In order to correlate the solution phase polymer chain conformation with the dry state hydrodynamic radii of MEH-PPV and CN-PPV were measured using fluorescence correlation spectroscopy (FCS). FCS was preferred over dynamic light scattering because of two distinct advantages. First, MEH-PPV and CN-PPV are inherently fluorescent and did not need fluorescent tagging. Second, the interference due to dust particles was negligible and simplifies the sample preparation. The following section describes the hardware, the experimental procedure and the results and discussion for FCS measurement.

5.1 Fluorescence Correlation Spectroscopy (FCS)

Fluorescence correlation spectroscopy (FCS) is a technique analogous to dynamic light scattering[60-62]. It is a statistical analytical method based on the fluctuations in fluorescence intensity about a mean fluorescence intensity, $\langle F(t) \rangle$, that can reveal non-equilibrium characteristics of the system. The fluctuations arise from the changes in the local concentration as fluorophores diffuse through the sampling volume and were autocorrelated as a function of time. Mathematically, the autocorrelation function for a fluorescent species with a fluorescence intensity of F(t) at a time t is given by the following equation:

$$G(\tau) = \frac{\langle \delta F(t).\delta F(t+\tau) \rangle}{\langle F(t) \rangle^2} \qquad (8)$$

Where δF(t) corresponds to the intensity fluctuation at time t, δF(t+τ) is the intensity fluctuation at some later time. For a single fluorescent species undergoing Brownian diffusion the autocorrelation function is the probability that a molecule at time t is in the laser volume after time t+τ.

In order to reduce background fluorescence, FCS measurements are generally performed on small focal volumes as defined by the focal spot at the detection optics. For a focused Gaussian beam, the observation volume in three dimensions takes the form of a prolate ellipsoid:

$$I(r) = I_0 \exp\left[\frac{-2(x^2 + y^2)}{r_0^2} - \frac{2z^2}{z_0^2}\right] \tag{9}$$

where r_0 is the beam radius and z_0 is the beam height in the axial direction. The autocorrelation function for a single fluorescent species diffusing through a three dimensional Gaussian intensity profile is given by:

$$G(\tau) = \frac{1}{N}\left(1 + \frac{\tau}{\tau_D}\right)^{-1} .\left(1 + \frac{\tau}{\omega^2 .\tau_D}\right)^{-1/2} \tag{10}$$

where τ is the time lag, $\omega = z_0/r_0$, N is the mean number of molecules and τ_D is the characteristic diffusion time in which the probe molecule resides in the focal volume of the laser. The diffusion coefficient, D is related to the characteristic diffusion time by $\tau_D = r_0^2 / 4D$. From the diffusion coefficient the hydrodynamic radius, R_h was obtained by substituting the value in Stokes-Einstein equation, $R_h = \frac{kT}{6\pi\eta_0 D}$ where, k is Boltzmann's constant, T is the temperature, and η_0 is the solvent viscosity.

The apparatus used for the experiment consisted of a Nikon TE2000 inverted microscope operating in epi-illumination mode [See figure 30]. 514.5nm line from an argon ion laser was used as the excitation source. The laser entered the microscope through the back port after spatial filtering and was directed into a high numerical aperture objective (Nikon 100x, 1.3NA) by a dichroic mirror. Fluorescence from the sample was collected by the same objective and was directed into a CCD camera (Micromax, Roper Scientific) for imaging or a high efficiency avalanche photodiode (APD, Perkin Elmer, SPCM-AQR-15) for single photon counting. A long pass filter (Melles-Griot) with a cut-on wavelength at 550nm and an interference bandpass filter (Omega Optical Inc.) were used to reduce background fluorescence. The signal from the APD was then sent to a correlator card (ALV-6010, ALV-Laser, Germany), which calculated the correlation function. A sample cuvette was constructed by attaching a glass cylinder to a glass coverslip with TorrSeal (Varian Vacuum Technologies). A rubber stopper was inserted into the cuvette to prevent solvent evaporation during data collection. Data was collected for MEH-PPV and CN-PPV in toluene, THF and DCM. A solution concentration of 10^{-11} M was used in all experiments.

Figure 31 shows autocorrelation curves for MEH-PPV solutions in DCM ($\diamond$), toluene ($+$) and THF ($\triangledown$). The curves were fitted with single diffusion coefficient model. The hydrodynamic radii (R_h) of MEH-PPV in DCM, toluene and THF from these curves were determined to be 2.6 nm, 15.5 nm and 29.5 nm respectively. Similar R_h values were found for CN-PPV in DCM (2.4 nm), Toluene (23.4) and in THF (44.5). That is, both MEH-PPV and CN-PPV adopt a more compact chain configuration in toluene relative to

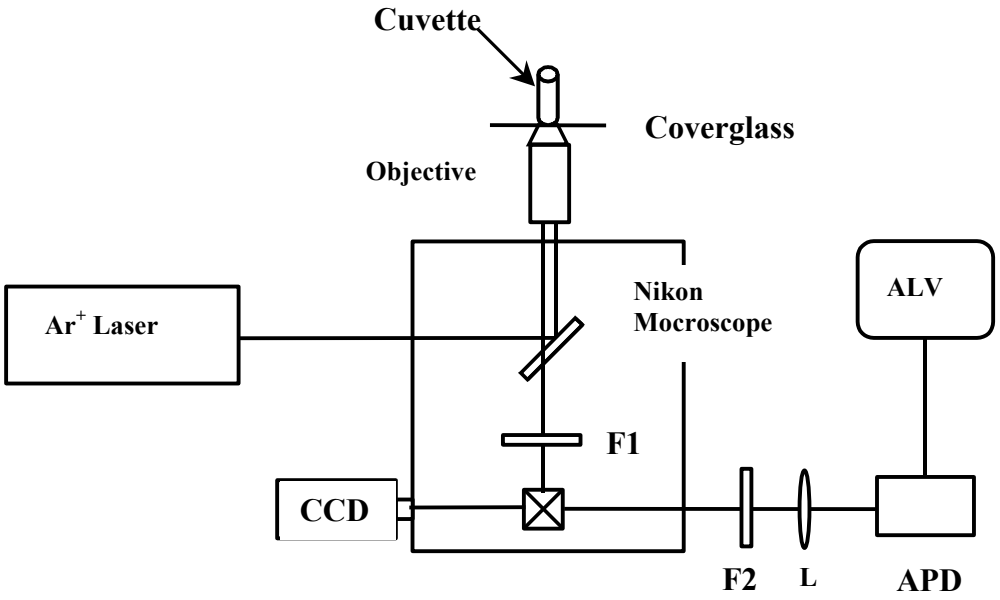

Figure 30. Schematic of FCS instrumentation.

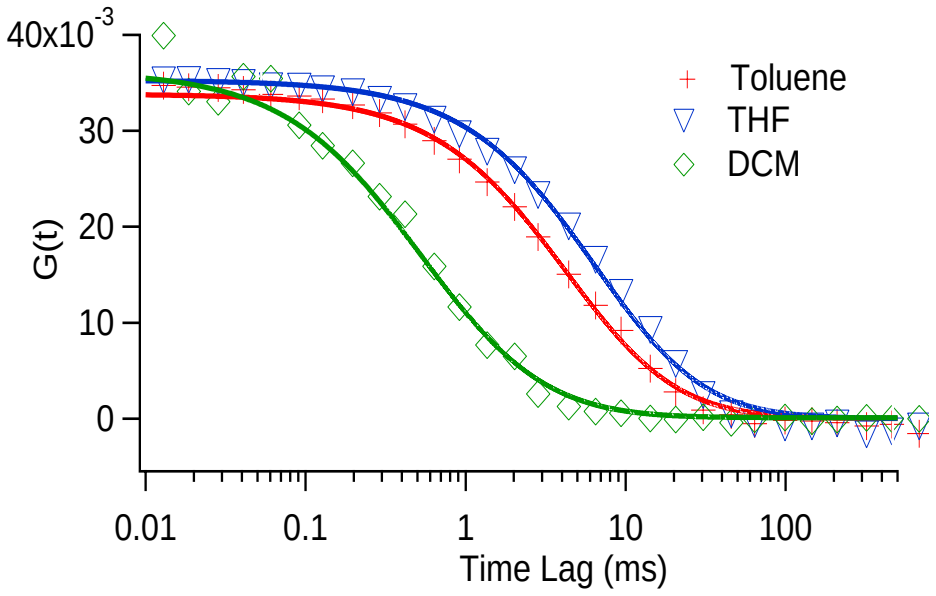

Figure 31. Fluorescence autocorrelation curves for freshly prepared solutions of MEH-PPV in DCM (◇), Toluene (+) and THF (▽). The corresponding hydrodynamic radii are 2.6 nm, 15.5 nm and 29.5 nm respectively. The solid lines are fit to the data to equation 3.

that in THF. The R_h values determined from analysis in DCM solution were unusually low (less than half of the persistence length) and are believed to result from an artifact resulting from multiple fluorescence events from different segments of a single polymer molecule. We believe that the polymer chains adopt a larger chain conformation in DCM than in THF or toluene solution and interpret the anomaly as follows. With an extended polymer chain conformation in DCM the conjugated segments in the polymer chain are relatively farther apart and this leads to inefficient energy transfer between the conjugated segments. As a result the polymer chains in DCM show multchromophoric behavior instead of single chromophoric behavior. Thus multiple fluorescence bursts are observed from a single polymer chain and the observed hydrodynamic radii of the polymer chain decreases rapidly.

The hydrodynamic radii also show a decrease with increase in solution concentration. We believe that this was an effect of fluorescence from multiple chains. The hydrodynamic radii of MEHPPV in Toluene decreased from 14.7 nm, to 8.3 nm to 7.14 as the concentration is increased from 10^{-12}M to 10^{-11}M to 10^{-10} M. This is analogous to the dynamic light scattering data reported by Schwartz and coworkers[10] where the reported hydrodynamic radii apparently decrease with concentration; an effect that was attributed to multiple scattering events from single chains.

5.2 Summary

Strong correlation was observed between the choice of the solvent and the preparation of z-oriented MEH-PPV and CN-PPV nanostructures. It was observed that z-oriented polymer nanostructures were conveniently prepared from a less polar solvent like toluene than from a more polar solvent like DCM. The hydrodynamic radii of MEH-PPV and

CN-PPV measured by fluorescence correlation spectroscopy, in toluene, THF and DCM, and the samples prepared from these solutions showed that the memory of polymer chain conformation in the solution is carried into the dry state nanoparticle. In the solution we observed that the polymer chains have a compact conformation in toluene relative to THF. Thus it was concluded that a compact chain conformation in solution facilitates the formation z-oriented nanostructures as opposed to a well extended solution phase chain conformation.

CHAPTER 6

Conclusions and Future Work

In this thesis I have shown that by using microdroplet techniques and proper use of solvents, substrates and sample preparation conditions morphology of single conjugated polymers can be controlled. Single molecules of MEH-PPV and CN-PPV deposited using microdroplet techniques on glass substrate show high internal structural order with the conjugated segments organized nearly parallel to each other and the transition moment oriented perpendicular to the substrate. Such structural organization and z-orientation of the polymer molecules resulted in markedly improved spectral and photophysical properties compared to bulk polymer. The results show narrow bandwidth emission, high photochemical stability and high photon count rates from z-oriented polymer molecules. By comparing the fluorescence lifetimes of CN-PPV in different environments, the effect of dielectric confinement and dipole orientation on the spontaneous emission was verified. Photon correlation measurement show definitive single photon emission z-oriented polymer molecules. In conclusion, by employing microdroplet techniques conjugated segments in a polymer chain can be organized nearly parallel to each other resulting in efficient energy transfer between the conjugated segments and the polymer chain behaves as a single photon source. With high photon count rate, high photochemical stability and single site emission, z-oriented polymer nanostructures can potentially be used as a single photon source for quantum information processing applications. The results open new avenues to be explored in terms of nanoscale application of conjugated polymers and future prospects appear bright.

Future work can be followed from the results obtained in this work. Future work can be focused on synthesizing oligomers and polymers with controlled conjugated segments in the polymer chain. If the results presented in this work holds true, then the use of a conjugated polymer whose conjugated segment length distribution is narrow (or no distribution), should emit at nearly constant wavelength. Conjugated polymers which are monodisperse in terms of conjugated segment distribution should be synthesized so that by using polymers of well defined conjugated segments, nanoscale photonic applications can be realized. Since the orientation of the polymer chain is very sensitive to the surface energy of the substrate, careful construction of designer substrates is also an immediate need to follow up on the present work.

LIST OF REFERENCES

(1) Lee, T. H.; Dickson, R. M. *Proceedings of the National Academy of Sciences of the United States of America* **2003**, *100*, 3043-3046.

(2) Misewich, J. A.; Martel, R.; Avouris, P.; Tsang, J. C.; Heinze, S.; Tersoff, J. *Science* **2003**, *300*, 783-786.

(3) Moerner, W. E.; Dickson, R. M.; Norris, D. J. *Mat Sci Eng B-Solid* **1997**, *48*, 169-174.

(4) Shen, Y.; Prasad, P. N. *Applied Physics B-Lasers and Optics* **2002**, *74*, 641-645.

(5) Gettinger, C. L.; Heeger, A. J.; Drake, J. M.; Pine, D. J. *J Chem Phys* **1994**, *101*, 1673-1678.

(6) Friend, R. H.; Gymer, R. W.; Holmes, A. B.; Burroughes, J. H.; Marks, R. N.; Taliani, C.; Bradley, D. D. C.; Dos Santos, D. A.; Bredas, J. L.; Logdlund, M.; Salaneck, W. R. *Nature* **1999**, *397*, 121-128.

(7) Hide, F.; DiazGarcia, M. A.; Schwartz, B. J.; Heeger, A. J. *Accounts Chem Res* **1997**, *30*, 430-436.

(8) Heeger, A. J. *J Phys Chem B* **2001**, *105*, 8475-8491.

(9) Nguyen, T. Q.; Yee, R. Y.; Schwartz, B. J. *Journal of Photochemistry and Photobiology a-Chemistry* **2001**, *144*, 21-30.

(10) Nguyen, T. Q.; Doan, V.; Schwartz, B. J. *J Chem Phys* **1999**, *110*, 4068-4078.

(11) Nguyen, T. Q.; Martini, I. B.; Liu, J.; Schwartz, B. J. *J Phys Chem B* **2000**, *104*, 237-255.

(12) Woo, H. S.; Lhost, O.; Graham, S. C.; Bradley, D. D. C.; Friend, R. H.; Quattrocchi, C.; Bredas, J. L.; Schenk, R.; Mullen, K. *Synthetic Metals* **1993**, *59*, 13-28.

(13) Schwartz, B. J. *Annu Rev Phys Chem* **2003**, *54*, 141-172.

(14) Nguyen, T. Q.; Kwong, R. C.; Thompson, M. E.; Schwartz, B. J. *Appl Phys Lett* **2000**, *76*, 2454-2456.

(15) Nguyen, T. Q.; Schwartz, B. J. *Journal of Chemical Physics* **2002**, *116*, 8198-8208.

(16) Nguyen, T. Q.; Wu, J. J.; Doan, V.; Schwartz, B. J.; Tolbert, S. H. *Science* **2000**, *288*, 652-656.

(17) VandenBout, D. A.; Yip, W. T.; Hu, D. H.; Fu, D. K.; Swager, T. M.; Barbara, P. F. *Science* **1997**, *277*, 1074-1077.

(18) Yu, J.; Hu, D. H.; Barbara, P. F. *Science* **2000**, *289*, 1327-1330.

(19) Hu, D. H.; Yu, J.; Barbara, P. F. *J Am Chem Soc* **1999**, *121*, 6936-6937.

(20) Hu, D. H.; Yu, J.; Wong, K.; Bagchi, B.; Rossky, P. J.; Barbara, P. F. *Nature* **2000**, *405*, 1030-1033.

(21) Hu, D. H.; Yu, J.; Barbara, P. F. *Abstracts of Papers of the American Chemical Society* **1999**, *218*, U381-U382.

(22) Schwartz, B. J.; Nguyen, T. Q.; Wu, J. J.; Tolbert, S. H. *Synthetic Met* **2001**, *116*, 35-40.

(23) Schaller, R. D.; Snee, P. T.; Johnson, J. C.; Lee, L. F.; Wilson, K. R.; Haber, L. H.; Saykally, R. J.; Nguyen, T. Q.; Schwartz, B. J. *J Chem Phys* **2002**, *117*, 6688-6698.

(24) Tolbert, S. H.; Wu, J. J.; Gross, A. F.; Nguyen, T. Q.; Schwartz, B. J. *Micropor Mesopor Mat* **2001**, *44*, 445-451.

(25) Collison, C. J.; Rothberg, L. J.; Treemaneekarn, V.; Li, Y. *Macromolecules* **2001**, *34*, 2346-2352.

(26) Nguyen, T. Q.; Kwong, R. C.; Thompson, M. E.; Schwartz, B. J. *Synthetic Met* **2001**, *119*, 523-524.

(27) Dickson, R. M.; Norris, D. J.; Moerner, W. E. *Phys Rev Lett* **1998**, *81*, 5322-5325.

(28) Dickson, R. M.; Norris, D. J.; Tzeng, Y. L.; Moerner, W. E. *Science* **1996**, *274*, 966-969.

(29) Moerner, W. E. *Science* **1994**, *265*, 46-53.

(30) Huser, T.; Yan, M.; Rothberg, L. J. *Proceedings of the National Academy of Sciences of the United States of America* **2000**, *97*, 11187-11191.

(31) Hu, D. H.; Yu, J.; Padmanaban, G.; Ramakrishnan, S.; Barbara, P. F. *Nano Lett* **2002**, *2*, 1121-1124.

(32) Hollars, C. W.; Lane, S. M.; Huser, T. *Chemical Physics Letters* **2003**, *370*, 393-398.

(33) Barnes, M. D.; Kung, C. Y.; Lermer, N.; Fukui, K.; Sumpter, B. G.; Noid, D. W.; Otaigbe, J. U. *Optics Letters* **1999**, *24*, 121-123.

(34) Barnes, M. D.; Ng, K. C.; Fukui, K.; Sumpter, B. G.; Noid, D. W. *Macromolecules* **1999**, *32*, 7183-7189.

(35) Barnes, M. D.; Ng, K. C.; Whitten, W. B.; Ramsey, J. M. *Analytical Chemistry* **1993**, *65*, 2360-2365.

(36) Kung, C. Y.; Barnes, M. D.; Lermer, N.; Whitten, W. B.; Ramsey, J. M. *Anal Chem* **1998**, *70*, 658-661.

(37) Bartko, A. P.; Dickson, R. M. *Journal of Physical Chemistry B* **1999**, *103*, 11237-11241.

(38) Bartko, A. P.; Dickson, R. M. *Journal of Physical Chemistry B* **1999**, *103*, 3053-3056.

(39) Mehta, A.; Thundat, T.; Barnes, M. D.; Chhabra, V.; Bhargava, R.; Bartko, A. P.; Dickson, R. M. *Applied Optics* **2003**, *42*, 2132-2139.

(40) Mehta, A.; Kumar, P.; Dadmun, M. D.; Zheng, J.; Dickson, R. M.; Thundat, T.; Sumpter, B. G.; Barnes, M. D. *Nano Letters* **2003**, *3*, 603-607.

(41) Kumar, P.; Mehta, A.; Dadmun, M. D.; Zheng, J.; Peyser, L.; Bartko, A. P.; Dickson, R. M.; Thundat, T.; Sumpter, B. G.; Noid, D. W.; Barnes, M. D. *Journal of Physical Chemistry B* **2003**, *107*, 6252-6257.

(42) Kung, C.; Barnes, M. D.; Lermer, N.; Whitten, W. B.; Ramsey, J. M. *Applied Optics* **1999**, *38*, 1481-1487.

(43) Bredas, J. L.; Cornil, J.; Beljonne, D.; dos Santos, D.; Shuai, Z. G. *Accounts Chem Res* **1999**, *32*, 267-276.

(44) Pradeep Kumar, S. M. M., Sheng Dai, Adosh Mehta, Mark D. Dadmun, Bobby G. Sumpter, and Michael D. Barnes. *Macromolecules* **2004**, *In press*.

(45) Kumar, P.; Lee, T. H.; Mehta, A.; Sumpter, B. G.; Dickson, R. M.; Barnes, M. D. *Journal of the American Chemical Society* **2004**, *126*, 3376-3377.

(46) Tae-Hee Lee, P. K., Adosh Mehta, Kewei Xu, Robert M. Dickson and Michale D. Barnes. *Applied Physics Letters* **2004**, *85*, 100-102.

(47) Pichler, K.; Halliday, D. A.; Bradley, D. D. C.; Burn, P. L.; Friend, R. H.; Holmes, A. B. *J Phys-Condens Mat* **1993**, *5*, 7155-7172.

(48) Chang, R.; Hsu, J. H.; Fann, W. S.; Liang, K. K.; Chiang, C. H.; Hayashi, M.; Yu, J.; Lin, S. H.; Chang, E. C.; Chuang, K. R.; Chen, S. A. *Chemical Physics Letters* **2000**, *317*, 142-152.

(49) Schniepp, H.; Sandoghdar, V. *Physical Review Letters* **2002**, *89*, -.

(50) Milonni, P. W. *The Quantum Vacuum*; Academic Press: New York, 1994.

(51) Barnes, W. L. *J Mod Optic* **1998**, *45*, 661-699.

(52) Chew, H. *Phys Rev A* **1988**, *38*, 3410-3416.

(53) de Dood, M. J. A.; Slooff, L. H.; Polman, A.; Moroz, A.; van Blaaderen, A. *Applied Physics Letters* **2001**, *79*, 3585-3587.

(54) de Dood, M. J. A.; Slooff, L. H.; Polman, A.; Moroz, A.; van Blaaderen, A. *Phys Rev A* **2001**, *6403*, -.

(55) Beveratos, A.; Kuhn, S.; Brouri, R.; Gacoin, T.; Poizat, J. P.; Grangier, P. *Eur Phys J D* **2002**, *18*, 191-196.

(56) Macklin, J. J.; Trautman, J. K.; Harris, T. D.; Brus, L. E. *Science* **1996**, *272*, 255-258.

(57) Lukosz, W.; Kunz, R. E. *Opt Commun* **1977**, *20*, 195-199.

(58) Twiss, R. H. B. a. R. Q. *Nature* **1956**, *178*, 1447.

(59) Kimble, H. J.; Dagenais, M.; Mandel, L. *Phys Rev Lett* **1977**, *39*, 691-695.

(60) Magde, D.; Elson, E. L.; Webb, W. W. *Biopolymers* **1974**, *13*, 29-61.

(61) Magde, D.; Webb, W. W.; Elson, E. *Phys Rev Lett* **1972**, *29*, 705-&.

(62) Mahurin, S. M.; Dai, S.; Barnes, M. D. *J Phys Chem B* **2003**, *107*, 13336-13340.

VITA

Pradeep K. Koyadankizhakkedath was born on July 29, 1971 in Kerala, India. He received his B. S. degree from University of Calicut, Kerala in 1993. He received M. S. degree in Organic Chemistry from Andhra University, Visakhapatnam in 1996 and M. S. degree in Polymer Science and Technology from Indian Institute of Technology, New Delhi in 1998. Then he came to the United States to complete his doctoral degree.